A cantilevered bistable piezoelectric harvester array for broadband vibration

Diankun Pan[1*], Zixin Yu[1], Zhuoyuan Qi[1], Zhangming Wu[1,2]

[1] Key Laboratory of Impact and Safety Engineering, Ministry of Education of China, Ningbo University, Ningbo, 315211, China
[2]School of Engineering, Cardiff University, Cardiff, CF24 3AA, Wales

Abstract: This paper presents a novel magnet-free nonlinear vibrational energy harvester array to broaden the operational bandwidth and improve power distribution across the bandwidth. This array consists of cantilevered bistable piezoelectric harvesters (CBPHs) with adjacent and interlaced bandwidths, each of which is capable of operating independently. Based on the nonlinear characteristics of the static mechanical properties of CBPHs, a lumped-parameter analytical model, which is characterized by a nonlinear spring connected in series with a linear spring, is developed to predict the dynamic responses. To lay the investigation foundation for array design, comprehensive dynamic analyses are performed on a representative CBPH, using experimental testing, finite element analysis, and the analytical model. Results show that the CBPH with weak bistability, characterized by a single load-displacement path, is more likely to exhibit a hardening-type nonlinear response with high output under a relatively low excitation level, which is desirable for broadband energy harvesting. Furthermore, a parametric analysis is conducted to establish the relationship between design parameters and mechanical properties, which can serve as a guideline for designing CBPHs. Guided by these insights, an array integrating five CBPHs is designed and fabricated. Under an acceleration level of 0.5 *g*, all CBPHs in this array exhibit broadband hardening-type responses, achieving an operational bandwidth of 18 Hz and a relatively uniformly distributed output power across this bandwidth with an average value of 0.65 mW. This performance outperforms that of the linear counterpart. Additionally, random vibration tests validate the array's adaptability across varying environmental vibrations, demonstrating its potential performance in practical applications.

Keywords: Piezoelectric; Energy harvesting; Bistable; Broadband; Nonlinear array; Cantilevered boundary

1. Introduction

In recent years, wireless sensor networks and mobile electronic platforms have become increasingly pervasive. Energy harvesters play a crucial role for sensors as they can serve as an independent power source [1, 2]. In particular, advancements in modern chip technology have substantially reduced the power requirements of integrated circuits and sensors, enabling low-power electronics to operate autonomously with the assistance of mechanical energy

*Corresponding author: pandiankun@nbu.edu.cn

harvesters [3-6]. Piezoelectric energy harvesters, which exploit the direct piezoelectric effect of piezoelectric materials, demonstrate outstanding electromechanical energy conversion efficiency, high energy density, and a simple operational mechanism [7-10]. They provide an effective means for harvesting mechanical vibrations [11, 12], transportation vibration [13, 14], or flow-induced vibration [15-17] and converting them into usable electric power, particularly in applications involving small dimensions or compact structures [18-20].

A conventional piezoelectric energy harvester typically employs a cantilever structure owing to its simplicity and ability to amplify small vibrations into larger displacements [21-23]. However, large power generation is generally limited to the beam's natural frequency, which may restrict the application for real-world variable-frequency vibration sources [24, 25]. Hence, it is crucial to design a broadband piezoelectric energy harvester for practical applications. Various strategies have been proposed to broaden the operational bandwidth, including multi-resonance arrays [26-29], internal resonance [30-34], frequency up-conversion [35-38], resonance tuning [39-42], and nonlinear techniques [43-48].

A linear harvester array with multiple resonant frequencies is a common method that has been utilized for broadband energy harvesting [49-51]. By carefully selecting the geometry of the harvesters and the tip masses, closely spaced resonant peaks can be achieved, thereby broadening the operational bandwidth. Upadrashata and Yang [52] proposed a novel trident-shaped multimodal piezoelectric energy harvester that achieves three close resonant peaks. Izadgoshasb *et al*. [27] optimized the shape of the cantilever beam in a multi-resonant piezoelectric energy harvester to suit the frequency range of the targeted vibration source. Kouritem *et al.* [53] adjusted the inclination angle of the tip masses in the piezoelectric beam array to effectively broaden the operational bandwidth. These linear energy harvester arrays demonstrate effective performance in enhancing the frequency bandwidth. However, to expand the bandwidth further, the sole option is to increase the number of beams, which may pose a limitation for applications with small-dimension requirements.

In the past few decades, nonlinear techniques have been widely utilized to broaden the operational frequency bandwidth, particularly through the integration of monostable [54, 55], bistable [56-60], tristable [61-64], or even multistable [65-67] structures into the design of piezoelectric energy harvesters. The methods for inducing nonlinearities primarily involve preloading or prestressing, which can be introduced through mechanical boundaries or magnetic forces [68-70]. These nonlinear energy harvesters, which typically integrate a single piezoelectric unit to achieve broadband operation, still may face challenges in terms of operational stability, risk resistance, and further improvement of output power and working bandwidth.

*Corresponding author: pandiankun@nbu.edu.cn

Inspired by linear multi-resonance arrays, an array configuration composed of multiple nonlinear energy harvesters is a promising strategy for further broadening the effective frequency bandwidth and improving operational stability. The common approach for these nonlinear energy harvester arrays is to utilize magnets that serve two functions: enhancing inertia and inducing nonlinearities. Upadrashta and Yang [71] proposed an array of nonlinear piezo-magnetoelastic energy harvesters for broadband vibration harvesting. Deng *et al*. [72] developed a poly-stable energy harvester array with interacting magnetic forces, which is capable of achieving multidirectional vibration energy harvesting across a broad frequency range. Lai *et al*. [73] presented a compact nonlinear multistable piezomagnetoelastic energy harvester array comprising tristable and monostable configurations, which can scavenge energy from low-amplitude, low-frequency vibrations. Mei *et al*. [74] proposed a nonlinear energy harvester array with one vertical and two horizontal piezoelectric beams, coupled by a magnetic-linkage effect for creating time-varying potential wells. Xie *et al.* [75] proposed a nonlinear piezoelectric coupled cantilever array that incorporates nonlinear magnetic forces to differentiate natural frequencies and broaden the energy harvesting bandwidth. While utilizing nonlinear magnetic interactions in energy harvester arrays can substantially boost performance by widening bandwidth and lowering excitation requirements, this approach still faces notable challenges. For instance, the dynamic responses and nonlinear magnetic interactions of these energy harvesters are highly sensitive to magnet arrangement. Moreover, the generated magnetic field may potentially interfere with the normal operation of adjacent electronic devices in magnetic-sensitive application scenarios, such as precision semiconductor metrology systems and aircraft avionics bays. Therefore, it is very necessary to develop high-performance nonlinear energy harvester arrays without employing magnets.

A potential approach to introduce nonlinearity into the energy harvester array without using magnets is to utilize assembled components, such as limiters and elastic supports. Fan *et al*. [76] developed a nonlinear piezoelectric energy harvester array comprising four cantilever piezoelectric beams and two motion limiters, which were utilized to achieve a nonlinear hardening frequency response. Shim *et al.* [77] proposed a nonlinear coupled piezoelectric beam array coupled by elastic supports to broaden the operational bandwidth and enhance harvesting performance. These nonlinear energy harvester arrays require additional components, which are not conducive to reducing the size of the array. Moreover, owing to the identical boundary constraints applied to all piezoelectric harvesters, it is challenging to adjust the nonlinearity of each beam independently.

In prior work, we proposed a magnet-free bistable piezoelectric broadband vibrational energy harvester [78], and demonstrated its fundamental dynamics and the feasibility of broadband energy harvesting. We found that a

*Corresponding author: pandiankun@nbu.edu.cn

hardening-type response delivers high output over a broader bandwidth, which is favorable for energy harvesting. However, on the hardening branch, output rises sharply with frequency, resulting in non-uniform power distribution across the effective bandwidth and limiting practical usability. Additionally, the excitation required to trigger this response was relatively high in our previous design. As a result, the performance of a single harvester, including bandwidth, output, and stability, is inherently limited. These limitations can be mitigated by using an array of multiple bistable harvesters with lower excitation requirements. Each harvester in the array is designed to have adjacent, interlaced hardening-type bandwidths, and this overlapping design balances power output and improves effective bandwidth coverage. Compared to the aforementioned nonlinear energy harvester array, this nonlinear energy harvester array offers two potential advantages: first, compared to the designs with magnetic-coupled mechanism, this array is suitable for the magnetic-sensitive scenarios, and the bistable harvesters in this array operate independently and the failure of one harvester does not affect the others, resulting in a higher anti-risk capability; second, compared to the designs with mechanical constraints, the required cantilever boundary condition enables a simple and flexible assembly method without the need for other components, which leads to a more compact structure and is more suitable for applications in compact spaces.

This work aims to develop a design strategy for nonlinear energy harvester arrays by adjusting the geometric parameters of this bistable harvester. Due to the structural complexity and multi-parameter nature of this bistable harvester, designing arrays with adjacent interlaced hardening bandwidths remains a challenge. To address this, two aspects of work are conducted: First, we analyze the fundamental dynamics of low-excitation bistable energy harvesters, and establish and validate a dynamic model based on the mechanical properties of bistable piezoelectric harvesters. The proposed model can effectively evaluate the dynamic performance of such harvesters. Second, a parametric analysis is performed to lay a foundation for harvester design. Finally, a nonlinear energy harvester array consisting of five bistable piezoelectric harvesters is designed and verified by experiments.

The remainder of this paper is structured as follows: Section 2 provides an overview of the fundamental conceptual design of the cantilevered bistable piezoelectric harvester. Section 3 describes the fabrication process and measurement procedures. Sections 4 and 5 present the investigation methodologies, including finite element analysis and an analytical model, respectively. Section 6 reports the results and provides a detailed discussion. Building upon these findings, Section 7 outlines the design and experimental characterization of the nonlinear energy harvester array. Finally, Section 8 summarizes the key conclusions.

*Corresponding author: pandiankun@nbu.edu.cn

2. Cantilevered bistable piezoelectric harvester

As the core component of the nonlinear energy harvester array, the bistable piezoelectric harvester consists of a laser-machined bistable host structure and piezoelectric transducers. As shown in Fig. 1(a), this bistable host structure has a typical monolithic planar configuration, featuring a rectangular shape with two symmetric rectangular slits along the longitudinal axis. The slits split the planar structure into a wider main beam (width W_1) and a pair of narrower supporting beams (width W_2), while the remaining portions serve to connect the three beams. The total structure length is L, and the slit length is L_1, which also equals the length of both the main beam and supporting beams. A 0.2 mm radius fillet is added at the slit corners to reduce stress concentration. After cutting this planar construction from a stainless steel thin plate by laser, the bistable structure can be obtained, as shown in Fig. 1(b). The laser-machining process cuts three closed polylines sequentially: finishing the two inner polylines forms two slits, and cutting the outer polyline separates the structure from the substrate. Residual stress in the heat-affected zone affects the supporting beams more significantly than the main beam, because the two heat-affected zones on the supporting beams are closer than those on the main beam. Even with identical laser parameters in single-step processing, deformation differs between the main beam and supporting beams due to their width difference. After the laser-machining process, the resulting deformation difference acts as axial compression applied to the main beam, giving the main beam bistability similar to a pre-compressed buckled beam supported by two tensioned strings, as shown in Fig. 1(b). By integrating constraints with a bistable buckled beam, this structure can be assembled with other components in a cantilever configuration, whose two stable bending states under the boundary condition are also presented in Fig. 1(b).

Integrating this bistable host structure with piezoelectric transducers realizes the bistable piezoelectric energy harvester, as shown in Fig. 1(c). Owing to the adoption of a cantilever boundary, two PZTs with length L_p and the same width as the main beam are bonded near the clamped end, as illustrated in Fig. 1(a) and (c). Two specific lengths ($L_{clamped}$ and L_{mass}) at both ends are set for attaching the boundary and tip mass. After bonding PZTs to the bistable structure, the boundary and tip mass are assembled to complete the cantilevered bistable piezoelectric harvester (CBPH), as illustrated in Fig. 1(c) and (d). The top view in Fig. 1(d) clearly distinguishes the two stable states by their bending directions, which can transition between each other by snap-through processes. When vibration at the clamped end triggers snap-through processes, CBPH effectively captures vibration energy and converts it to electricity.

*Corresponding author: pandiankun@nbu.edu.cn

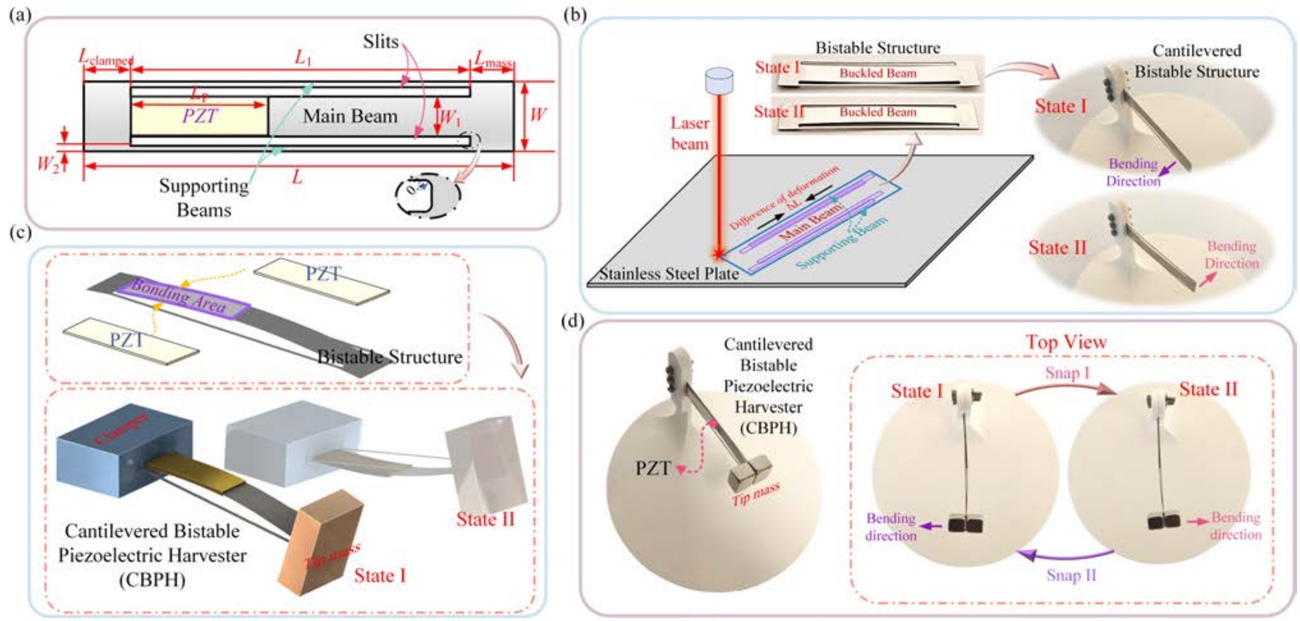

Fig. 1 Concept design of CBPH: (a) The planar geometric diagram of the bistable host structure; (b) The manufacturing process of the bistable host structure and its two stable states under the cantilevered boundary condition; (c) The schematic diagram of CBPH composed of the bistable host structure and piezoelectric transducers and the three-dimensional diagram of two stable states of CBPH with tip mass; (d) The CBPH experimental sample and its two stable states in the top view.

3. Experiments

3.1 Fabrication

Bistable host structures were fabricated from stainless steel plates via a laser processing system, with laser parameters selected based on prior experimental experience: average power 960 W, scanning speed 330 mm/s. During fabrication, nitrogen-assisted gas coaxial with the laser beam was delivered through a conical nozzle. After completing two inner loops, the outer loop was cut, and the full structure was separated from the substrate, as shown in Fig.1(b). The presence and degree of bistability depend on two factor categories: laser processing parameters and geometric parameters. To streamline manufacturing and cut production costs, a single laser recipe enables a more efficient integrated preparation process, so this study only focuses on parametric analysis of the structure's geometric parameters. Subsequently, after the bistable structure was fabricated, two PZTs with a thickness of 0.2 mm were precisely bonded to designated areas on the surface of the main beam using cyanoacrylate adhesive, resulting in the formation of the bistable piezoelectric harvester sample. The geometric parameters for a representative bistable piezoelectric harvester are listed in Table 1.

*Corresponding author: pandiankun@nbu.edu.cn

Table 1. Geometric parameters of the bistable piezoelectric harvester

Component	Geometric parameters	Symbol	Values (mm)
Bistable host structure	Length of the main beam	L_1	40
	Length of the clamped side	L_{clamped}	5
	Length of the tip side	L_{mass}	5
	Total width	W	8
	Width of the main beam	W_1	5
	Width of the supporting beam	W_2	0.8
	Thickness of the steel plate	t_{s}	0.25
Piezoelectric transducer	Length of PZT	L_{p}	20
	Width of PZT	W_{p}	5
	Thickness of PZT	t_{p}	0.2

3.2 Experimental measurements

To evaluate the bistability degree of the CBPH sample, a quasi-static experiment was conducted to capture force-displacement responses during its snap-through processes between two stable states. The experimental setup is shown in Fig. 2(a). The sample was clamped to a support frame to form a cantilever boundary condition, with its free end connected to a load sensor with an accuracy of 1 mN. The load sensor is fixed on a motor-driven movable stage that allows controlled forward and backward movement, and a laser sensor monitors the stage's movement and captures its displacement. As the stage moves, the sample produces snap-through processes, and the corresponding load and displacement data are recorded simultaneously by a program, generating load-displacement curves for the two snap-through processes. To maintain the quasi-static condition, the stage moved at a speed of 4 mm/min.

Following the aforementioned static measurement, a dynamic measurement was conducted after attaching a tip mass to the free end of the CBPH sample to lower the fundamental frequency and increase the inertia, as shown in Fig. 2(b). The employed dynamic experimental system consists of an electromagnetic shaker, a controller with the function of signal generation, a power amplifier, and an oscilloscope, as depicted in Fig. 2(c). The sample is fixed on the shaker, which is driven by the power amplifier and controller to generate harmonic vibration. An accelerometer mounted on the shaker measures real-time acceleration and feeds data back to the controller, forming a computer-controlled closed-loop system for frequency-sweep testing under a set acceleration level. In both forward and reverse frequency sweep tests, an oscilloscope measured the open-circuit voltage of parallel-connected piezoelectric elements, and this voltage-frequency response is used to evaluate the dynamic performance of the CBPH sample. In addition, a laser sensor was used to measure the displacement response at a specific single frequency to characterize vibration modes combined with voltage responses.

*Corresponding author: pandiankun@nbu.edu.cn

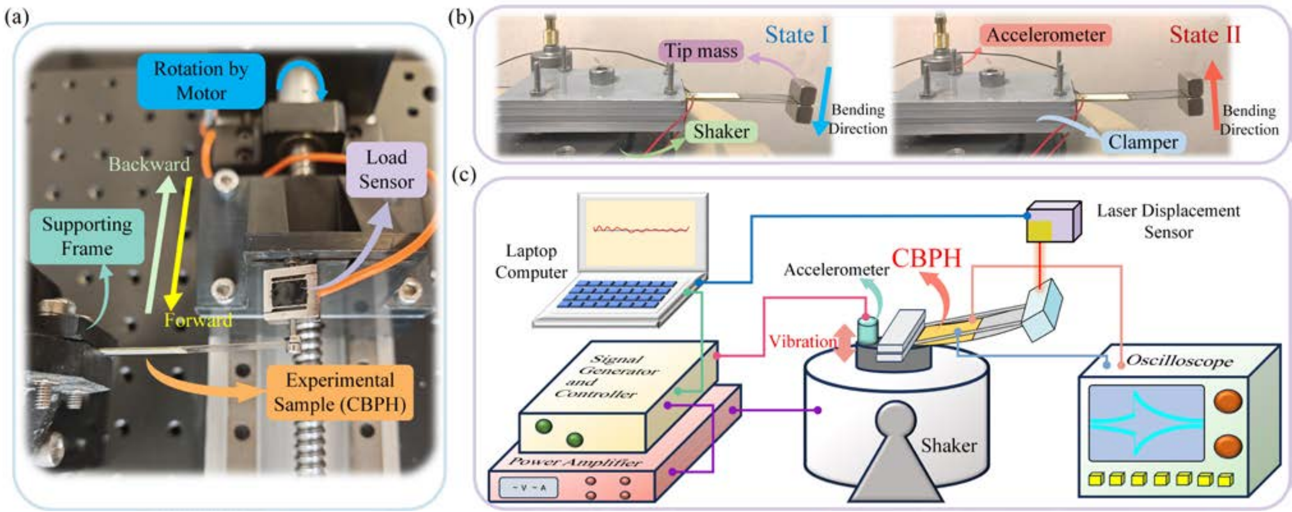

Fig. 2. The experimental measurements: (a) The experimental setup for the static measurement of force-displacement curves during two snap-through processes; (b) The typical two stable states of the experimental sample assembled on the shaker; (c) The experimental setup for the dynamic measurement for CBPH.

4. Finite element analysis

4.1 Static analysis

The finite element analysis (FEA) is conducted using the commercial software ABAQUS. The shell element S4R and the piezoelectric solid element C3D20E are utilized to model the bistable structure and PZTs, respectively. The PZTs are attached to the designated bonding regions on the surface of the main beam by applying a ‘tie’ constraint during the assembly process. The electric potential on the bonded surfaces of the PZTs is fixed at zero for the duration of the analysis, while a uniform electric potential is obtained from the free surfaces using equation constraints. Geometrically nonlinear algorithms are enabled by activating the ‘Nlgeom’ switch for the entire duration of the analysis. Material properties are listed in Table 2. A convergence study and efficiency analysis have been performed to determine an optimal mesh size of 0.5 mm.

A static finite element analysis is conducted to characterize the mechanical characteristics of the CBPH, including stable states and snap-through behavior. This simulation focuses on the post-fabrication stable state; thus, it does not fully cover residual stress evolution and transient physical effects during laser machining. Meanwhile, the adopted assumption is that the residual stress does not vary over time, and neither the material anisotropy nor the variation of the laser heat-affected zone is taken into account. To generate the deformation difference between the main beam and the supporting beams, a specific temperature field characterized by a negative equivalent temperature gradient ΔT is applied as an initial condition to the regions representing the supporting beams in the finite element model. All degrees of freedom on the clamped side are constrained during analysis to establish cantilever boundary conditions.

*Corresponding author: pandiankun@nbu.edu.cn

Two ‘static, general’ steps are needed to obtain the stable state: a nominal lateral displacement is applied to the tip end as a disturbance in the first step, then the disturbance is removed in the second step to achieve the stable state. To trigger the snap-through process from the current stable state to another, a lateral displacement opposite to the initial disturbance is applied to the tip in the third step. The reaction force is extracted together with displacement to construct a force-displacement curve, which is used to characterize the nonlinear mechanical properties and is subsequently compared with experimental results to quantify the degree of bistability.

In the finite element model, the degree of bistability depends on the applied temperature gradient ΔT. As shown in Fig. 3, when ΔT is 0, the force-displacement curve is nearly linear. As ΔT increases, nonlinearity grows, and bistability emerges. The degree of bistability can be estimated by the maximum force and the tip displacement corresponding to stable states. Higher snapping force and larger tip displacement lead to stronger bistability, making the snap-through process harder to trigger. Furthermore, the hysteresis response becomes pronounced when bistability is sufficiently strong. However, this temperature gradient ΔT remains unknown and must be determined based on experimental results.

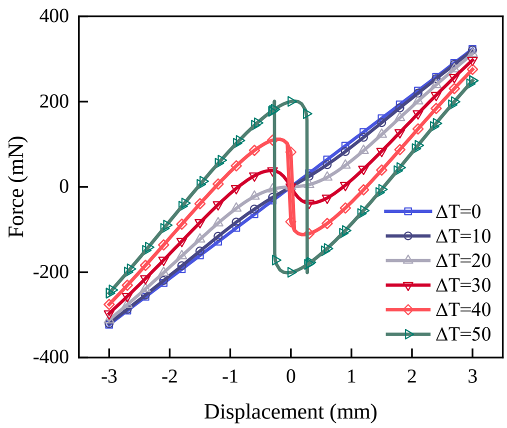

Fig. 3. The force-displacement curves under different temperature gradients ΔT predicted by FEA.

Table 2. Material properties used in the finite element analysis.

Material	Properties
Steel	Density ρ=7900 kg/m^3 Elastic modulus E_s=197.5 GPa Poisson’s ratio v=0.28 The coefficient of thermal expansion α=14.4×10^{-6}/°C
PZT	Density ρ=7600 kg/m^3 Modulus E_p=61 GPa Poisson’s ratio v=0.3 Piezoelectric constants d_{31}=−270×10^{-12} m/V, d_{33}=550×10^{-12} m/V Permittivity ε=3400ε_0, ε_0=8.85×10^{-12} F/m

When bistability is pronounced, snap-through behavior is hard to trigger, making it challenging to obtain the high-

*Corresponding author: pandiankun@nbu.edu.cn

output interwell response [70, 79]. However, for energy harvesting, practical ambient vibration sources typically have low excitation intensity. Thus, selecting weakly bistable systems with lower excitation requirements is a more favorable design choice. Based on prior research experience [80], a CBPH with weak bistability is selected to demonstrate core performance characteristics. Five bistable host structure specimens were fabricated under identical processing conditions, and their force-displacement responses during snap-through were measured. The mean force-displacement curves and corresponding variance are shown in Fig. 4(a). The consistent curves and small variance confirm the repeatability and stability of this laser-machined bistable host structure. Based on the experimental results, the equivalent temperature gradient ΔT for FEA is set as 27 °C. It should be emphasized that this value is empirical, and it can reflect the degree of bistability, but it does not capture the quantifiable physical correlation between laser processing parameters and the material properties of the heat-affected zone. The force-displacement curves obtained from FEA match well with experimental data, proving that using a reasonable equivalent temperature gradient in the finite element model is an effective and feasible method. Next, three specimens were fabricated for the CBPH. Their mean experimental force-displacement curves with variance are compared to FEA predictions, as shown in Fig. 4(b), demonstrating the stability and repeatability of the CBPH. The CBPH's force-displacement response follows a single equilibrium path independent of snap-through direction, resembling a classical bistable system governed by a cubic equation. However, the rising segment has a less steep slope than the descending segment, distinguishing it from typical classical bistable system behavior.

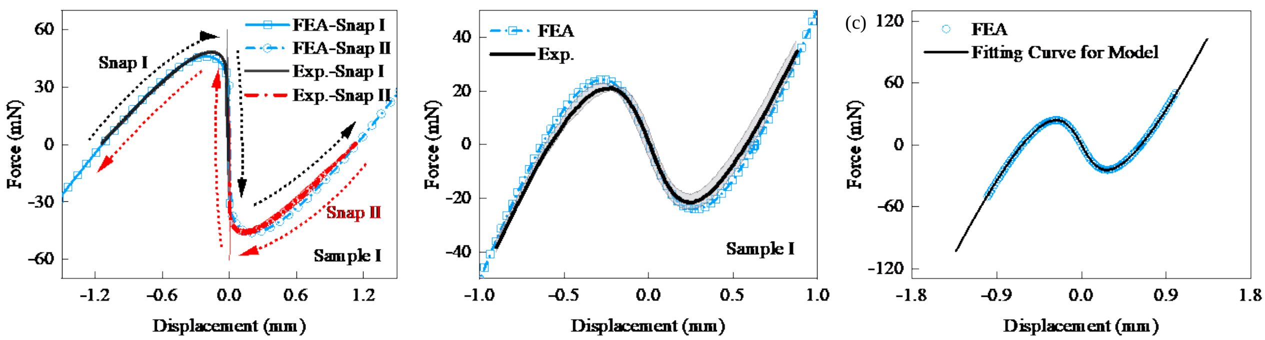

Fig. 4 (a) The experimental and FEA-predicted force-displacement curves during two snap-through processes of the bistable host structures; (b) The experimental and FEA-predicted force-displacement curves during snap-through processes of CBPH; (c) The force-displacement curves fitted by three stiffness coefficients compared with the results of FEA.

After the above static finite element analysis, a perturbation analysis step is introduced after the attainment of State I. Within this analysis step, the Lanczos solver integrated within the finite element solver is utilized to compute the first-order vibration mode and corresponding natural frequency, with a 5 g inertial mass simultaneously applied at the tip side. The first-order vibration mode is a bending mode, with a natural frequency of 24.6 Hz. Based on this

*Corresponding author: pandiankun@nbu.edu.cn

result, the frequency sweep range in experiments can be set from 7 Hz to 35 Hz to cover the primary dynamic responses.

4.2 Dynamic analysis

To capture the dynamic response characteristics of the CBPH, the simulation first applies two 'static, general' steps to obtain a stable state, followed by a 'dynamic, implicit' analysis step. For comparison with experimental results, two types of dynamic simulations are performed: frequency-sweep analysis under a specified acceleration level and single-frequency vibration response evaluation. To simulate harmonic frequency-sweep excitation with a certain acceleration, the excitation signal is generated by

$$Amp = A\sin(2\pi(f_0 t + \frac{1}{2}kt^2)) \tag{1}$$

where A is the amplitude of acceleration, f_0 is the starting frequency of the sweep, k is the frequency sweep rate, and t represents the time that the dynamic analysis step takes. This acceleration signal, which is input to the 'Tabular Amp' function in ABAQUS, is applied to the clamped side of the CBPH to simulate the frequency-sweep response. Then, the voltage responses from both forward and reverse sweeping under identical acceleration are obtained, which can be compared with experimental results. Additionally, both forward and reverse sweeping are conducted under identical acceleration conditions. To investigate typical vibration modes, a harmonic displacement excitation at a specific frequency is applied to the clamped side in a separate 'dynamic, implicit' step. The voltage responses under different vibration modes are captured in the time domain. Additionally, the tip displacement responses are obtained by eliminating the influence of the excitation signal, enabling a comparison with the experimental results.

5. Analytical model

While finite element models yield reliable dynamic analysis results, the 'dynamic implicit' step makes simulations time-consuming, especially for frequency-sweep analyses that take over ten hours. Thus, an effective simplified analytical method is essential for predicting dynamic response. Based on Hamilton's principle, the governing equations of a lumped-parameter model for a typical bistable piezoelectric energy harvester can be written as,

$$\begin{cases} m\ddot{x}(t) + c\dot{x}(t) + F_r - \theta v(t) = F(t) \\ C_p\dot{v}(t) + v(t)/R + \theta\dot{x}(t) = 0 \end{cases} \tag{2}$$

where m and c are the equivalent mass and damping, respectively; θ is the equivalent electromechanical coupling coefficient; C_p is the equivalent capacitance of the piezoelectric transducer; R is the load resistance; $v(t)$ is the voltage across the electrical load resistance; $x(t)$ is the relative displacement of the mass to the base; $F(t)$ is the external

*Corresponding author: pandiankun@nbu.edu.cn

excitation force; F_r is the equivalent nonlinear restoring force. In this model, the nonlinearity of the bistable system predominantly arises from the term F_r. For the typical Duffing system, the restoring force F_r is given by,

$$F_r = -k_1 x + \alpha x^3 \tag{3}$$

where k_1 and α are the stiffness coefficients to describe the nonlinear mechanical properties of this system. The corresponding typical force-displacement curve is illustrated in Fig. 5(a), where the equilibrium position x_0 corresponding to zero force and the snapping force F_{max} are determined by the coefficients k_1 and α. Given known values of x_0 and F_{max}, these two coefficients can be uniquely determined. Thus, x_0 and F_{max} can also serve as effective parameters for characterizing this bistable system.

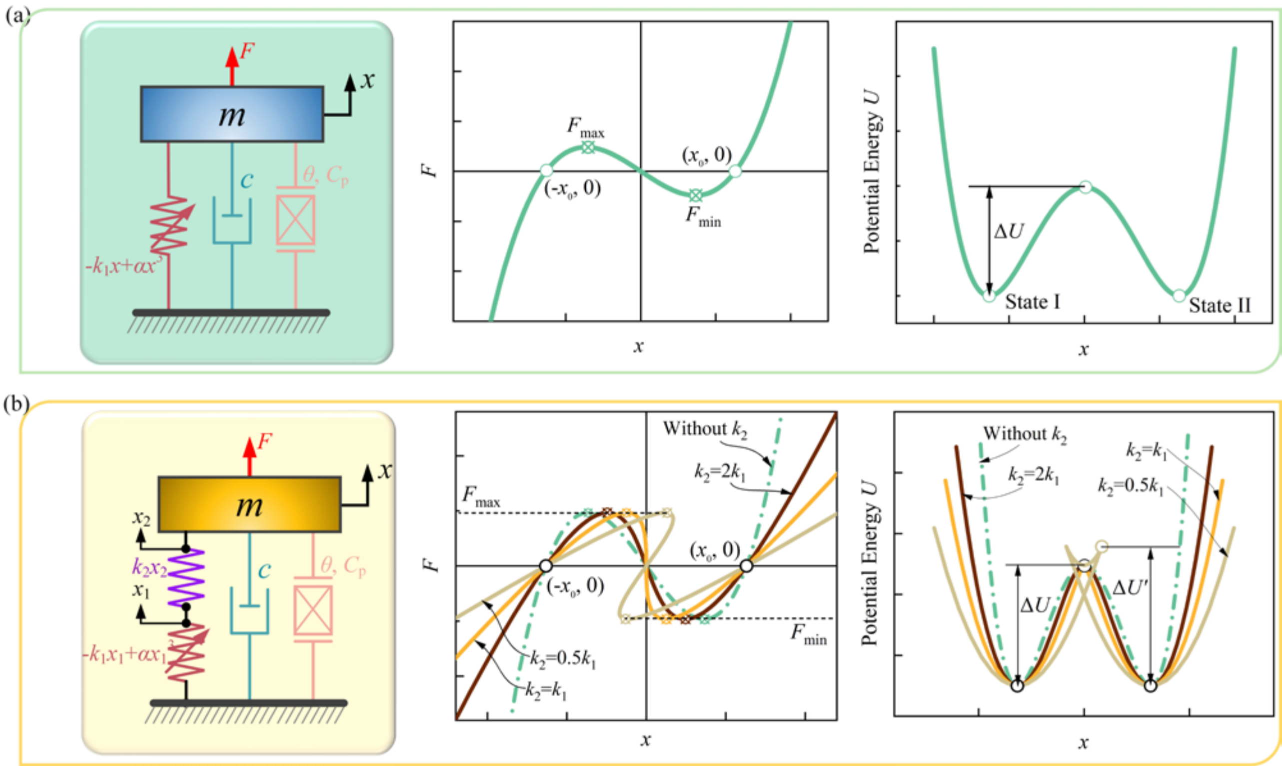

Fig. 5 (a)The typical dynamic model for a bistable piezoelectric energy harvester based on the Duffing system and the corresponding restoring force-displacement curve; (b) The dynamic model for the proposed CBPH developed by incorporating a linear spring in series with the nonlinear spring and the corresponding restoring force-displacement curves under varying linear stiffness values.

For the proposed CBPH, the force-displacement curve trend differs from that of the typical Duffing system discussed earlier. The response shows softening behavior: its rising segment is longer than the descending segment. Owing to the complexity of the force-displacement curve, polynomial fitting is commonly used to obtain stiffness coefficients and derive the expression for F_r [78]. However, this method impedes parametric analysis because the coefficients are fitted for specific conditions. In addition, more complex force-displacement behavior requires higher-order polynomials to reach sufficient fitting accuracy. In this study, a simplified model is proposed by modifying the

*Corresponding author: pandiankun@nbu.edu.cn

Duffing equation, based on the force-displacement curve characteristics of the CBPH. Inspired by the von Mises truss system with spring-connected loading [81], a linear spring of stiffness k_2 is added to the system and connected in series with the existing nonlinear spring, as shown in Fig. 5(b). Let the extensions of the linear and nonlinear springs be x_2 and x_1, respectively, which gives the restoring force F_r as:

$$F_r = k_2 x_2 = -k_1 x_1 + \alpha x_1^3 \tag{4}$$

The nonlinear and linear springs are coupled in series under the same force F_r, and their deformation adds up to the system's total deformation x, so the restoring force F_r can be expressed by x, as follows,

$$F_r = -k_1(x - F_r/k_2) + \alpha(x - F_r/k_2)^3 \tag{5}$$

The plots of F_r against x are shown in Fig. 5(b), for varying spring stiffness k_2 at fixed k_1 and α. While curve shapes change with k_2, the stable position x_0 and force F_{max} stay constant. When k_2 is twice the value of k_1, the rising segment is longer than in the case without k_2, and the overall trend matches that of the CBPH shown in Fig. 4(b). As k_2 decreases, the slope of the rising segment gradually reduces, and the displacement growth reverses. When k_2 is half of k_1, the curve exhibits a positive slope in the descending branch, and this phenomenon is referred to as snapback. From the viewpoint of energy, the potential energy U of the system is,

$$U = -\frac{1}{2}k_1 x_1^2 + \frac{1}{4}\alpha x_1^4 + \frac{1}{2}k_2(x - x_1)^2 \tag{6}$$

The stability condition could be expressed by,

$$\frac{\partial^2 U}{\partial x_1^2} > 0 \tag{7}$$

So the critical stability condition is,

$$\frac{\partial^2 U}{\partial x_1^2} = -k_1 + 3\alpha x_1^2 + k_2 = 0 \tag{8}$$

Then, the critical deformation x_{10} of the nonlinear spring could be obtained through the above equation, and the critical deformation x_{01} corresponding to the snapback point could be obtained by adding the corresponding x_2, as follows,

$$x_{01} = x_{10} + \frac{-k_1 x_{10} + \alpha x_{10}^3}{k_2}, \quad x_{10} = \sqrt{\frac{k_1 - k_2}{3\alpha}} \tag{9}$$

From the critical value x_{10}, it can be observed that the force-displacement curve of the system displays a single equilibrium path when k_2 exceeds k_1, suggesting a potential criterion for system behavior. Moreover, the potential energy curves are obtained, as depicted in Fig. 5. In the Duffing system, state transitions occur only when the energy barrier ΔU is overcome. The addition of the linear spring k_2 leaves ΔU unchanged, provided there is no snapback.

*Corresponding author: pandiankun@nbu.edu.cn

However, the occurrence of snapback raises the barrier to $\Delta U'$ and hinders state transitions. Thus, the snapback phenomenon should be avoided, and the single-path force-displacement response is favorable when designing the CBPH with weak bistability.

The above analysis demonstrates that adjusting the three stiffness parameters, k_1, α, and k_2, enables an accurate representation of the force-displacement behavior of the CBPH across various nonlinear mechanical characteristics. Since the coefficient k_2 does not influence the equilibrium position x_0 or the maximum force $F_{\max}$, which is determined by the coefficients k_1 and α, it is straightforward to determine k_1 and α based on the values of x_0 and $F_{\max}$ predicted by FEA. Subsequently, k_2 can be fine-tuned until the fitted curve aligns with the FEA results. Using this method, the stiffness coefficients for the CBPH are determined, as presented in Table 3, and the resulting fitting curves are compared with FEA results in Fig. 4(c). The curve is well characterized by the three stiffness coefficients and shows good agreement with the FEA results.

Table 3. Parameters for the analytical model

Parameters	Values
Equivalent mass m	0.0057 kg
Equivalent damping coefficient c	0.030 Ns/m
Equivalent capacitance C_p	1.6×10^{-8} F
Equivalent electromechanical coupling coefficient θ	9.0×10^{-5} N/V
Stiffness coefficients of the restoring force	k_1=99.3 N/m, α=2.49×10^{8} N/m^3, k_2=260 N/m

This work focuses on the CBPH with relatively weak bistability, which is almost characterized by a single force-displacement curve. This case, which does not involve the snapback phenomenon, can be governed by equations as follows,

$$\begin{cases} m\ddot{x}(t)+c\dot{x}(t)-k_1x_1(t)+\alpha x_1(t)^3-\theta v(t)=F(t) \\ -k_1x_1(t)+\alpha x_1(t)^3-k_2(x(t)-x_1(t))=0 \\ C_p\dot{v}(t)+v(t)/R+\theta\dot{x}(t)=0 \end{cases} \tag{10}$$

Here, the variable $x_1(t)$ is the displacement of the nonlinear spring. The remaining parameters utilized in these equations are summarized in Table 3. To accurately identify the system’s dynamic properties, a ring-down free vibration test was conducted by mechanically plucking the sample to induce a small-amplitude oscillation. The mechanical damping coefficient was directly extracted from the resulting transient displacement response using the logarithmic decrement method. Concurrently, the electromechanical coupling coefficient was determined by analyzing the proportional relationship between the generated open-circuit voltage and the simultaneous tip displacement recorded during the same free-decay period. Additionally, the internal capacitance of the piezoelectric

*Corresponding author: pandiankun@nbu.edu.cn

elements was experimentally measured using an impedance analyzer. The numerical simulation using the 'NDSolve' command of Mathematica was used to obtain the results of the model. To obtain the frequency sweep results, the excitation force $F(t)$ is derived from the acceleration signal and the known mass. For single-frequency excitation, $F(t)$ takes the form of a harmonic function.

6. Results and discussion

6.1 Frequency sweep results

Linear frequency sweeps are conducted bidirectionally for the CBPH over the frequency range from 7 Hz to 35 Hz at a sweep rate of 30 Hz/min. The open-circuit voltage outputs under two acceleration levels (0.1 g and 0.2 g, where g=9.8 m/s^2) are obtained via three methods: analytical modeling, experimental testing, and finite element analysis, as illustrated in Fig. 6. Overall, the results predicted by FEA and the model show good agreement with the experimental results.

At an acceleration of 0.1 g, a fluctuating peak dominates the response in the forward frequency sweep, indicating inter-well vibration exhibiting snap-through behavior, as shown in Fig. 6(a). In the reverse frequency sweep, the main response bandwidth is significantly narrowed. Notably, the FEA results are obtained from a dynamic analysis step appended to a preceding static analysis step. As a result, the piezoelectric transducer was subjected to a certain level of stress induced by the buckling of the main beam prior to this dynamic analysis, which leads to a non-zero initial output voltage. For the frequency sweep processes, the forward sweep starts from State I with a positive voltage, and the state remains unchanged after the snap-through behavior. In contrast, the reverse sweep stabilizes at State II with a negative voltage after a single snap-through behavior.

When acceleration reaches 0.2 g, the primary fluctuating response further broadens in the forward frequency sweep. In the reverse sweep, the primary response includes two branches: the hardening-type branch and the fluctuating-type branch, as shown in Fig. 6(b). The hardening-type branch features rising voltage with increasing frequency, making it especially suitable for energy harvesting due to its high output and wide bandwidth. Experimental results show its frequency range is 10.6 Hz to 18.4 Hz. Beyond this branch, the fluctuating-type branch extends to higher frequencies, reaching 22.2 Hz in experiments. For FEA predictions, regardless of the direction of the frequency sweep, the system stabilizes at State II upon completion of the frequency sweep.

The above results show that both finite element analysis and the analytical model accurately predict the fundamental dynamic behavior of CBPH. However, the finite element method is computationally intensive for simulating

*Corresponding author: pandiankun@nbu.edu.cn

frequency-sweep responses. In contrast, the analytical model can predict the system's dynamic characteristics much faster, which is its main advantage. As shown in Fig. 7, two extra experimental acceleration levels (0.05 *g* and 0.35 *g*) are used to validate the analytical model. At 0.05 *g* excitation, the dynamic response shows softening behavior with the resonance peak shifting to lower frequencies during the forward frequency sweep. In the reverse sweep, this softening behavior becomes more pronounced, accompanied by snap-through behavior observed in both experimental and modeling results. When the excitation level rises to 0.35 *g*, a hardening-type response is also observed in the forward frequency sweep, with the corresponding frequency band further broadened. Notably, an extra fluctuating branch corresponding to a superharmonic response appears at lower frequencies before the hardening-type behavior starts.

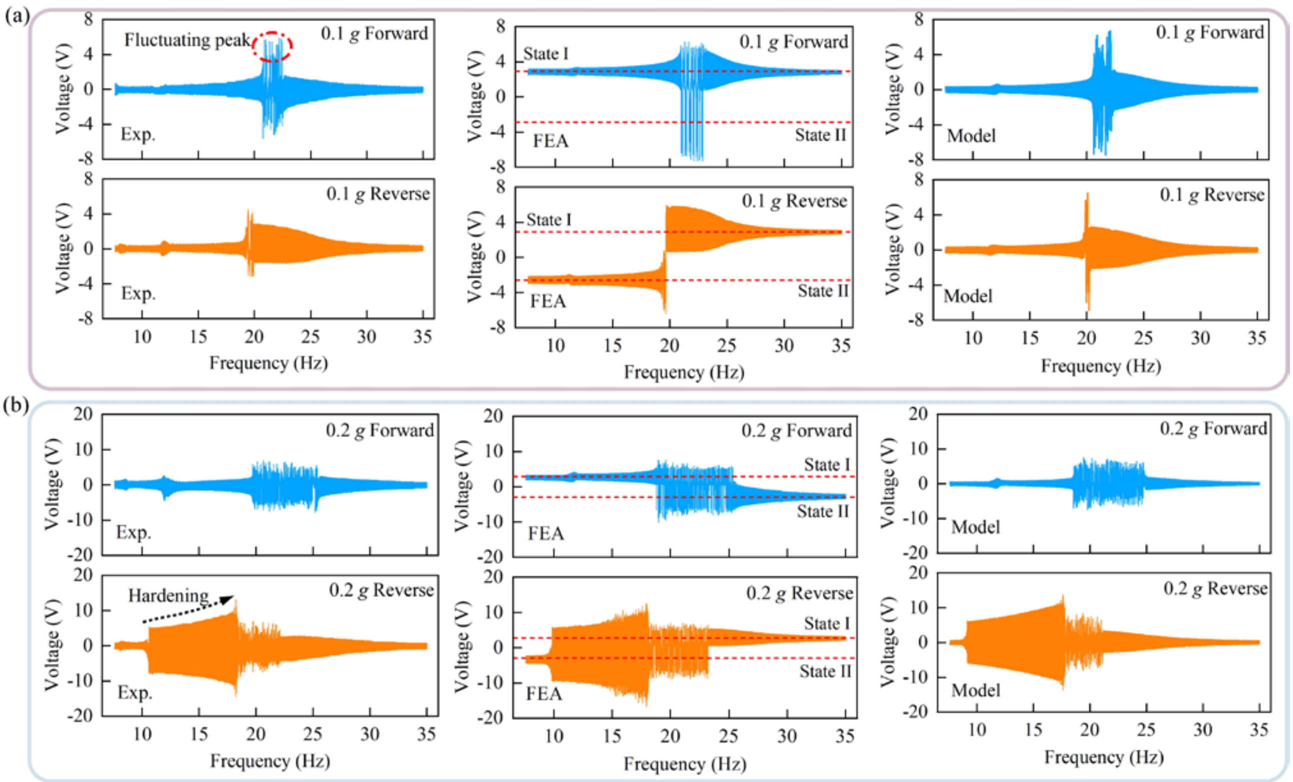

Fig. 6 Voltage-frequency responses under varying excitation levels obtained from experimental measurements, finite element analysis, and the model: (a) the acceleration level is 0.1 *g*, and (b) the acceleration level is 0.2 *g*.

*Corresponding author: pandiankun@nbu.edu.cn

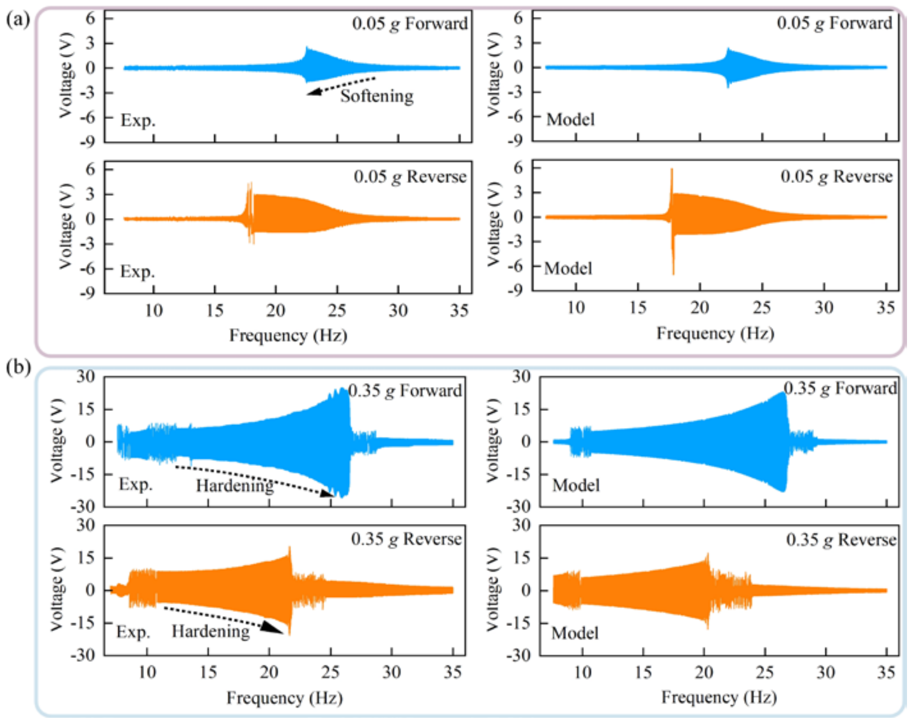

Fig. 7 Voltage-frequency responses under varying excitation levels obtained from the model and experimental measurements: (a) the acceleration level is 0.05 *g*, and (b) the acceleration level is 0.35 *g*.

Comparing frequency-sweep results in two directions, an apparent discrepancy is observed in the bandwidth locations of hardening branches. This discrepancy comes from the hysteretic behavior caused by the system's inherent nonlinearity, leading to a staggered bandwidth arrangement. The vibration mode on the hardening branch is interwell vibration with high-orbit characteristics. Transitioning to this mode from low-energy intrawell vibration requires accumulating enough energy to overcome the potential energy barrier. Thus, the lower frequency limit of the hardening branch in forward frequency sweep is relatively high, and this mode persists due to inertia until the energy accumulated in one cycle can no longer sustain it. In reverse frequency sweep, transitioning from intrawell to interwell vibration also needs energy accumulation, so its onset frequency is lower than the upper frequency in forward sweep, and this mode persists down to a lower frequency. Furthermore, under the same acceleration, reverse sweep is more likely to induce this interwell vibration, as shown in Fig. 6(b). This is because the vibration initiation during reverse sweeps stems from energy accumulated by high-frequency intermittent interwell vibration. In forward sweeps, by contrast, the intermittent interwell vibration after large-amplitude interwell vibration contributes no energy accumulation.

The frequency-sweep results show that the proposed model effectively and accurately predicts fundamental nonlinear dynamics. This analytical model provides a computationally efficient method to predict CBPH's dynamic behavior and determine their effective bandwidth across varying mechanical properties, defined by three stiffness coefficients.

*Corresponding author: pandiankun@nbu.edu.cn

6.2 Vibration modes

To further illustrate the nonlinear dynamic characteristics of CBPH, the typical vibration modes are examined. When snap-through behavior is not triggered and the system oscillates within a single potential well, the motion is defined as intrawell vibration, a common observation in frequency sweep results. Vibrational modes at frequencies away from the primary peak are typically intrawell vibration. A representative response at 15 Hz and 0.2 *g*, shown in Fig. 8(a), illustrates this mode. Fast Fourier Transform (FFT) analyses based on time-voltage data confirm that the dominant response frequency matches the excitation frequency. Additionally, a weak 30 Hz harmonic component is observed, indicating the nonlinear characteristic of CBPH.

In energy harvesting applications, the interwell vibration mode is more desirable and attractive than the intrawell mode owing to its higher output, particularly when snap-through behavior can be sustained continuously [78, 82]. This interwell vibration mode typically occurs along the hardening-type branch. As shown in Fig. 8(b), a typical interwell vibration featuring continuous snap-through behavior is observed at 0.2 *g* acceleration and 19 Hz frequency. The symmetry of the time-displacement curves about zero indicates that the system alternates regularly between its two stable states. The voltage response, which exhibits a relatively high amplitude, is primarily harmonic, with only minor fluctuations superimposed on the fundamental waveform. The FFT plot shows that the snap-through frequency of the primary response matches the excitation frequency, which is the defining characteristic of this vibration mode. The observed fluctuations correspond to harmonic components at integer multiples of the excitation frequency.

Besides the two periodic vibration modes, chaotic interwell vibrations are often found on the fluctuating-type branch. Fig. 8(c) shows a representative chaotic response at 21 Hz with 0.2 *g* acceleration to demonstrate this mode. The displacement and voltage signals are irregular, and amplitude variations prove that snap-through behaviors occur. The FFT plot shows a response component matching the excitation frequency, while the continuous frequency band below 60 Hz confirms chaotic characteristics. The superharmonic response is observed when the acceleration level increases to 0.35 *g*, which is another typical vibration mode. A representative case of this mode under 0.35 *g* and 12 Hz excitation is shown in Fig. 8(d). The displacement signal shows that snap-through behavior is not triggered, and the waveform remains regular. The voltage signal shares a similar waveform with the displacement signal, and corresponding FFT plots indicate that the harmonic response at twice the excitation frequency is comparable to the main response induced by excitation.

*Corresponding author: pandiankun@nbu.edu.cn

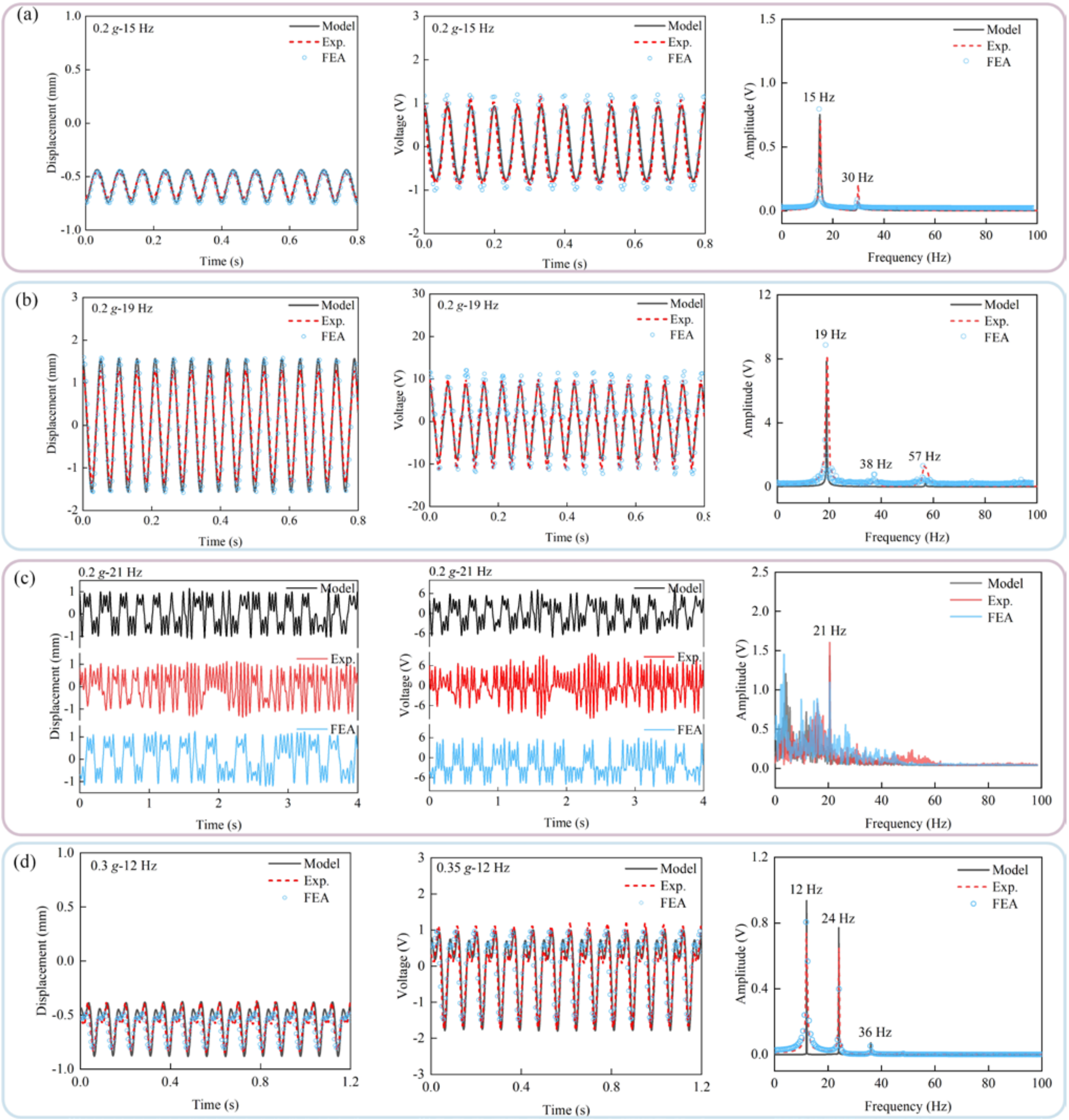

Fig. 8 Typical vibration modes described by the time-displacement curves, time-voltage curves, and FFT plots, obtained from the model, experimental measurements, and finite element analysis: (a) Typical intrawell vibration mode under the excitation condition of 0.2 *g* and 15 Hz; (b) Typical interwell vibration mode with continuous snap-through behavior under the excitation condition of 0.2 *g* and 19 Hz; (c) Typical chaotic interwell vibration mode under the excitation condition of 0.2 *g* and 21Hz; (d) The harmonic vibration mode under excitation condition of 0.35 *g* and 12 Hz.

6.3 Output power

The output powers are further characterized through experiments. In this process, a full-wave rectifier circuit is utilized to connect the CBPHs to the load resistance. The RMS (Root-Mean-Square) voltages in the two frequency-

*Corresponding author: pandiankun@nbu.edu.cn

sweeping directions are acquired under different load resistance conditions. The RMS voltage-frequency responses corresponding to different load resistances at an acceleration level of 0.35 g are presented in Fig. 9(a) and (b). The RMS voltage exhibits a nonlinear increase with the load resistance, resulting in a relatively optimized load resistance of 196 kΩ with higher RMS powers, as depicted in Fig. 9(c) and (d).

Due to the hardening-type response, RMS power increases substantially with frequency. On the hardening branch, the maximum power is 0.61 mW in the forward sweep, and the minimum is 0.05 mW, which is twelve times lower than the maximum. The average power across the hardening branch is 0.14 mW, resulting in notable power nonuniformity across the effective bandwidth. Similar behavior occurs in the reverse sweep, but the power nonuniformity is less pronounced than in the forward sweep. Furthermore, the power associated with the intermittent interwell vibration is also significantly lower than that of the hardening branch. Therefore, the frequency range corresponding to the hardening branch represents the primary effective bandwidth for energy harvesting. During the forward sweep, its effective bandwidth is wider than 10 Hz. When considering the PZT volume and the excitation level, its maximum power density is 124.5 mW·cm^{-3}·g^{-2}, but the average power density decreases to 28.6 mW·cm^{-3}·g^{-2}.

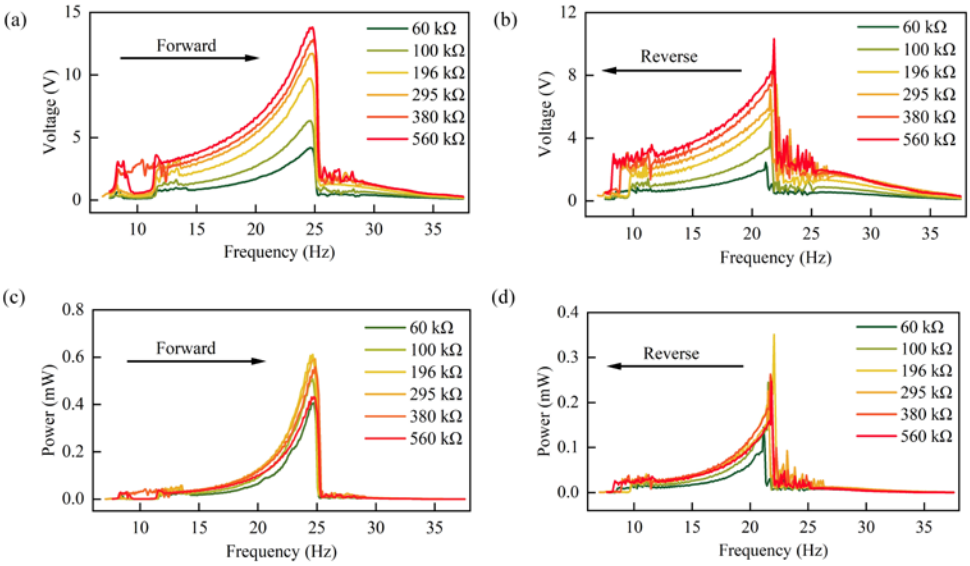

Fig. 9. The output responses of Sample I associated with different load resistances under the excitation level of 0.35 g: (a) Voltage-frequency response in the forward sweep; (b) Voltage-frequency response in the reverse sweep; (c) Power-frequency response in the forward sweep; (d) Power-frequency response in the reverse sweep.

In summary, the CBPH with a weak bistability is beneficial for achieving a wider effective bandwidth for energy harvesting under relatively low excitation. However, the non-uniformity of power across the effective bandwidth of a single CBPH results in relatively poor performance in real applications. To overcome this limitation, arranging multiple CBPHs with adjacent, interlaced effective bandwidths in an array is a potential solution to broaden

*Corresponding author: pandiankun@nbu.edu.cn

bandwidth and improve power uniformity.

6.4 Parametric analysis

To lay a foundation for designing a nonlinear energy harvester array incorporating several CBPHs, it is necessary to know the varying tendencies of the geometric parameters on its nonlinear characteristics. Here, five geometric parameters, including L, L_p, W_1, t_s, and W_2, are given priority to consider in this section. A series of static finite element models is constructed to obtain force-displacement curves for different geometric combinations. Subsequently, the nonlinear mechanical properties characterized by the snapping force and the tip displacement corresponding to each stable state are extracted from the force-displacement responses obtained during the snap-through process. Throughout the parametric analysis, the basic geometric parameters remain consistent with those listed in Table 2.

As illustrated in Fig. 10(a), the influence of the total length L of the CBPH is first investigated with three different lengths of PZT. Since the equivalent temperature field remains constant, bistability may disappear when L is too short, as the load required to induce buckling in the main beam increases with decreasing L. When bistability is present, the snapping force and tip displacement increase with L simultaneously, which is explained by the fact that an increase in L enhances the buckling degree of the main beam, while the cantilever boundary contributes to the increase in tip displacement. Further results concerning L_p are presented in Fig. 10(b). As observed, the bistability vanishes when L_p becomes excessively long, since the increased L_p enhances the stiffness of the main beam and raises the critical buckling load, thereby preventing buckling deformation. For the bistable cases, the snapping force and tip displacement initially decrease slightly, then exhibit a significant increase before ultimately declining with further increases in L_p. This phenomenon can be attributed to the following mechanism: when L is held constant, an increase in L_p not only mitigates the degree of buckling, but also improves the flexural stiffness of the structure under the cantilever boundary. This combined effect of the two factors gives rise to the observed trend.

*Corresponding author: pandiankun@nbu.edu.cn

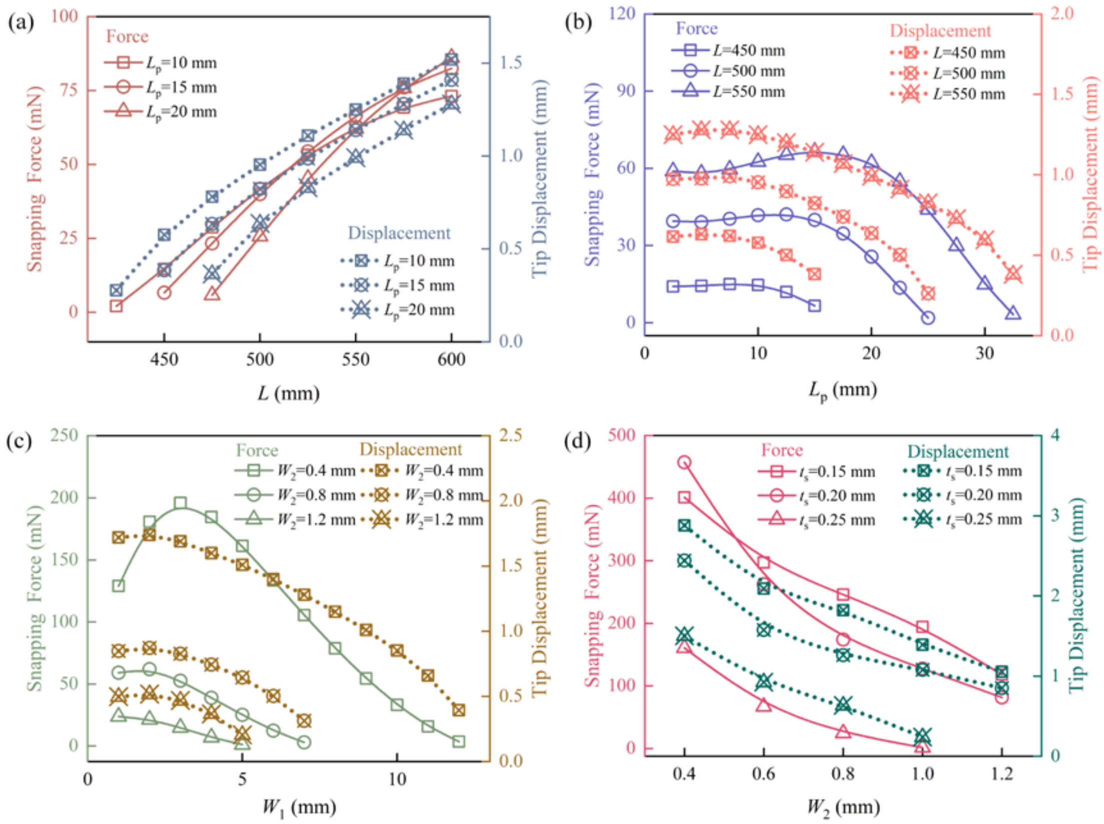

Fig. 10 The snapping force and tip displacement associated with different geometric parameters obtained from the FEA prediction: (a) The total length L associated with the three lengths L_p of PZT; (b) the length L_p of PZT associated with three lengths L; (c) The width W_1 of the main beam associated with the three widths W_2 of supporting beams; (d) the width W_2 of supporting beams associated with three thicknesses t_s of the substrate.

Based on the mechanism of the bistable host structure, bistability arises from the differential deformation between the main beam and the supporting beams. This deformation difference is regulated by the width W_2 of the supporting beams and the thickness t_s of the steel plate, which act as critical factors governing the bistable behavior of the structure. To quantify the combined effects of W_2 and t_s, a series of experimental specimens was fabricated and tested to obtain their force-displacement curves during snap-through transitions. It is observed that, for samples with identical parameters, the equivalent temperature gradient ΔT converges to a stable value when FEA predictions are consistent with experimental results. As illustrated in Fig. 11, these empirically obtained ΔT values can be used in the finite element model for subsequent analysis of W_1, W_2, and t_s. It is noted that, when t_s is held constant, the equivalent temperature gradient ΔT decreases nonlinearly with increasing W_2. This phenomenon can be explained as follows: increasing W_2 gradually separates the two laser-induced heat-affected zones on the supporting beams further apart, which reduces the differential deformation between the main beam and supporting beams and, in turn, decreases the buckling extent of the main beam. When W_2 is constant, increasing t_s makes it more difficult for the main beam to buckle. However, the laser-induced residual stress is limited, and it cannot supply enough compressive

*Corresponding author: pandiankun@nbu.edu.cn

load to induce buckling behavior for the thicker beam. Therefore, under the same manufacturing conditions, the degree of bistability gradually weakens until the bistability disappears with increasing t_s. The temperature gradient ΔT is utilized to quantify the degree of bistability, so the temperature gradient ΔT decreases as t_s increases.

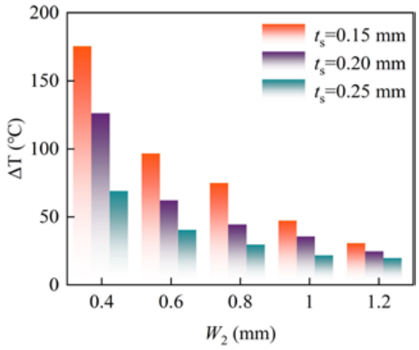

Fig. 11. The equivalent temperature gradients used in the finite element model associated with different widths W_2 of supporting beams and thicknesses t_s of the host structure.

The snapping force and tip displacement are assigned to different values of W_1 under three distinct W_2 values, as illustrated in Fig. 10(c). When W_2 is held constant, both the snapping force and tip displacement initially increase and then decrease as W_1 increases, and this trend is more pronounced for the snapping force. The reason for this tendency is similar to that of parameter L_p. Furthermore, three thickness t_s values of the host structure are considered in combination with three different values of W_2, as shown in Fig. 10(d). Under the same geometric conditions, inducing bistability becomes progressively more difficult as t_s increases. When bistability exists, for a fixed t_s, the snapping force and tip displacement decrease approximately monotonically as W_2 increases.

Based on the parametric analysis presented above, it is observed that the nonlinear mechanical properties, including snapping force and tip displacement, are jointly determined by two factors: the buckling degree of the main piezoelectric beam and the cantilever boundary condition. The buckling degree of the main piezoelectric beam is determined by the width W_2. Due to the cantilever boundary, parameters such as W_1, t_s, L, and L_p can modify the flexural mechanism under the tip load, in addition to adjusting the buckling degree of the main beam. The degree of buckling dictates the difficulty of initiating snap-through behavior, while flexural stiffness determines the position of the primary dynamic response peak. For instance, when other parameters are determined, the length L serves as an effective parameter for adjusting the bandwidth location, and the width W_2 can be utilized to adjust the bistability.

Furthermore, as previously discussed, the CBPH exhibiting weak bistability, characterized by a single force-displacement path, is a favorable configuration for achieving a hardening-type response in energy harvesting under relatively low excitation levels. Therefore, identifying geometric parameter combinations that yield a single force-displacement path can effectively enable the realization of the desired dynamic response for energy harvesting

*Corresponding author: pandiankun@nbu.edu.cn

applications. For instance, by analyzing the effects of L and L_p, it is evident that increasing L_p while keeping L constant, or decreasing L while maintaining L_p unchanged, effectively produces the desired single force-displacement path for CBPH.

7. Nonlinear energy harvester array

7.1 Design

This paper primarily aims to present a nonlinear piezoelectric energy harvester array using the proposed CBPHs. The CBPHs in the array should exhibit adjacent and interlaced primary response peaks that can collectively form a continuous and effective bandwidth. To simplify fabrication, all CBPHs use the same thickness, allowing monolithic integration from a single steel substrate by one-step laser processing. All CBPHs are also required to have a hardening-type response to broaden effective bandwidth and boost output. Additionally, all CBPHs in the array must operate simultaneously, meaning they activate via the hardening-type response at the same excitation level, such as 0.5 g.

Based on the previous parametric analysis, five CBPHs are identified that meet the requirements for constructing the nonlinear energy harvester array. A thickness of 0.25 mm is chosen first for t_s, as prior experience shows it helps obtain weak bistability. The supporting beam width W_2 is selected as the key parameter to tune the CBPHs' bistability. Next, the length L and width W_1 are determined following the trends from the parametric analysis to adjust the location of the effective bandwidth. Stiffness coefficients are extracted from FEA results, and the analytical model simulates frequency-sweep responses to check whether the requirements are met. Finally, five CBPHs are confirmed, with their geometric parameters and stiffness coefficients summarized in Table 4.

According to the stiffness coefficients, the force-displacement curves of five CBPHs are compared in Fig. 12(a). For CBPH-1#, which exhibits the highest snapping force, the bistability is relatively strong, and the force-displacement curve displays a weak snapback phenomenon. The remaining CBPHs exhibit a single force-displacement path, with CBPH-2# showing the lowest snapping force. Notably, the slope of the rising segment of the force-displacement curves progressively increases from CBPH-1# to CBPH-5#, indicating that the stiffness of the five CBPHs is staggered.

*Corresponding author: pandiankun@nbu.edu.cn

Table 4. The geometric parameters and stiffness coefficients of CBPHs in the nonlinear energy harvester array

	Geometric parameters				Stiffness coefficients		
	L_1/mm	W_1/mm	W_2/mm	Size of PZT/mm	k_1/N/m	α/×10^8 N/m^3	k_2/N/m
CBPH-1#	45	3	1.0	20×3	136.9	1.46	120.0
CBPH-2#	40	3	1.2	20×3	125.4	5.33	180.0
CBPH-3#	40	5	0.8	15×5	138.2	2.16	245.0
CBPH-4#	35	5	0.6	15×5	125.6	3.19	370.0
CBPH-5#	30	5	0.4	15×5	124.2	3.26	550.0

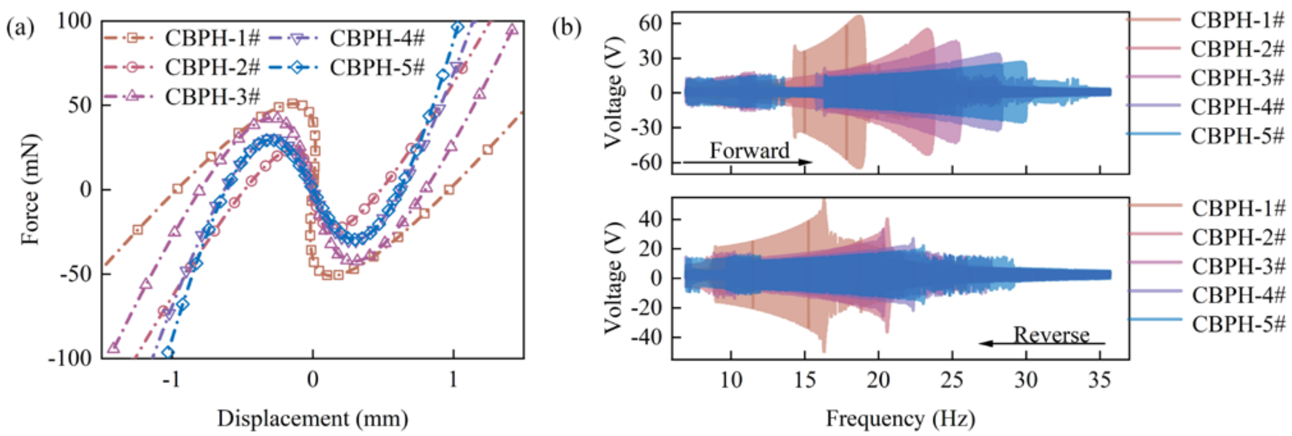

Fig. 12 (a) Force-displacement curves of five CBPHs in the array controlled by the three types of stiffness coefficients; (b) The voltage-frequency results of five CBPHs in two sweep directions at an acceleration of 0.5 *g* evaluated by the model.

While stiffness coefficients are already determined, the equivalent electromechanical coupling coefficient and equivalent damping coefficient remain unknown and are usually obtained experimentally. Due to the relatively weak electromechanical coupling effect, the location of the bandwidth is dominated by stiffness coefficients. Two reference values based on experimental experience are adopted for the electromechanical coupling coefficient and a damping ratio, respectively, which are 1.2×10^{-4} N/V and 0.015. The mass is retained, while the equivalent capacitance is estimated based on the geometric area of the piezoelectric transducer. As a result, the frequency-sweep response of five CBPHs can be roughly estimated using the model, as shown in Fig. 12(b). At an acceleration of 0.5 *g*, all five CBPHs exhibit typical hardening-type nonlinear behavior in the forward sweep direction, with their effective bandwidths distributed in an adjacent and interlaced manner, which means that multiple CBPHs can enter into interwell response at a single frequency. Specifically, the hardening-type response branches from CBPH-1# to CBPH-5# collectively span a frequency range from 14.3 Hz to 30.3 Hz. In the reverse sweep, this operational range shifts toward lower frequencies, and the staggered distribution of the hardening branches becomes less distinct. Notably, the response curves of CBPH-2# and CBPH-3# nearly overlap. These modeling results show that integrating five CBPHs into a broadband nonlinear energy harvester array is feasible, and the adjacent interlaced bandwidth

*Corresponding author: pandiankun@nbu.edu.cn

distribution helps improve output uniformity.

7.2 Fabrication and measurements

Next, to verify the design of this nonlinear energy harvester array, an experimental sample was fabricated. Five CBPHs with identical thickness were integrated into a monolithic array, and the host structure, consisting of five cantilevered bistable host structures, was cut from a steel substrate through a single laser cutting process, as shown in Fig. 13(a). After bonding PZTs and assembling the assembly with clampers and tip masses, a nonlinear energy harvester array composed of five CBPHs was obtained, as shown in Fig. 13(b). To eliminate the effects of aerodynamic damping coupling and mechanical crosstalk transmitted through the shared base, the spacing between adjacent harvesters is designed to be sufficiently large, and the mounting clamps are designed to be sufficiently rigid. A linear energy harvester array was also fabricated as a counterpart. For comparability, the main piezoelectric beam of the CBPH was kept identical to the linear piezoelectric beam (LPB), and the five-beam host structure was cut by laser using the same process, as shown in Fig. 13(c). To obtain continuous bandwidth for this linear array, the tip mass of each LPB is adjusted. After bonding the PZT and assembling the tip masses, the linear array shown in Fig. 13(d) is completed.

Due to the nonlinear large-deformation dynamic behavior of CBPH, the output voltage and current of each CBPH in the array vary dynamically over time, leading to considerable instantaneous amplitude differences among individual CBPHs. To eliminate charge cancellation caused by phase inconsistency on the AC side, each CBPH is equipped with an independent full-bridge rectifier circuit. After rectification, the DC sides can also be connected in series or in parallel. However, for DC series connection, the total loop current is limited by the unit with the weakest instantaneous output, which induces significant power loss under nonlinear operating conditions. For DC parallel connection, output currents from individual channels are summed. This connection exhibits stronger tolerance to unbalanced outputs of different CBPHs, and failure of a single CBPH will not disable the entire array. Therefore, the array adopts the circuit of independent rectification followed by DC parallel connection, as shown in Fig. 13(e). A filtering capacitor (C_f) of 3.3 μF is incorporated to smooth the DC voltage output, and a resistor R serves as the terminal load. Based on the measured voltage output and the value of the connected resistor, the output power of the array can be calculated. The same measurements are also carried out for the linear array.

*Corresponding author: pandiankun@nbu.edu.cn

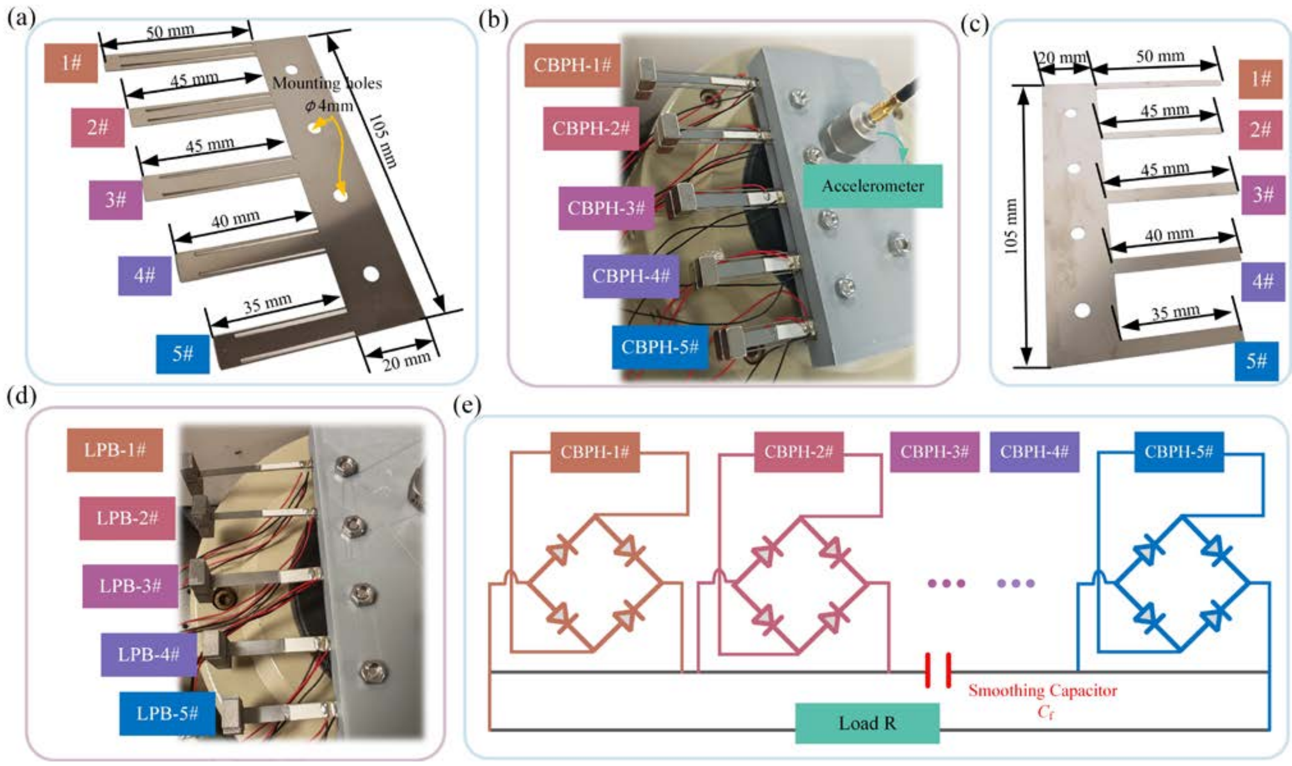

Fig. 13 (a) The monolithic host structure consisted of five bistable host structures fabricated by laser technique for the nonlinear energy harvester array; (b) The nonlinear energy harvester array consisted of five CBPHs mounted on the shaker; (c) The host structure with five cantilevered beams for the linear energy harvester array; (d) The linear energy harvester array consisted of five linear piezoelectric beams mounted on the shaker; (e) The parallel connection of five CBPHs in the nonlinear energy harvester array during measurement.

7.3 Frequency-sweep performance

Frequency-sweep measurements were conducted on the array to verify its broadband characteristics. As shown in Fig. 14(a), the power-frequency curves for various load resistances in the forward direction were obtained under an excitation level of 0.5 *g*. The forward-sweep curves show five adjacent continuous hardening-type peaks corresponding to the five CBPHs. The main response region covers a wide effective bandwidth, approximately 15 Hz to 33 Hz, giving the nonlinear array a total operational bandwidth of 18 Hz, which demonstrates its potential for broadband energy harvesting. This experimental effective frequency range and bandwidth basically agree with the estimation by the model. Therefore, the design objective of this nonlinear energy harvester array has been successfully verified. When the load resistance varies, the output power also changes. The average power within the effective bandwidth is used as an evaluation metric for determining the optimal resistance. It is found that the average power output at 295 kΩ is relatively high, reaching 0.65 mW, which is approximately half of the peak power of CBPHs. Compared with the previous single CBPH, the array effectively improves power distribution. Calculated by the array's total PZT volume, the average power density is 18.8 mW·cm^{-3}·g^{-2}, lower than the single CBPH because not

*Corresponding author: pandiankun@nbu.edu.cn

all arrayed CBPHs operate simultaneously. However, calculated by average PZT volume per CBPH, the average power density reaches 94.2 mW·cm^{-3}·g^{-2}, which is significantly higher than the single device. This performance improvement comes from adjacent interlaced bandwidths that allow multiple CBPHs to operate synergistically and boost output.

During reverse frequency sweeps shown in Fig. 14(b), the array exhibits a degraded main response region and lower average power, and the average power within the bandwidth of 13 Hz to 30 Hz decreases to 0.30 mW under the resistance condition of 295 kΩ. Three distinct response peaks are evident, but experimental observations indicate that all CBPHs exhibit continuous interwell vibration responses. This occurs because the hysteresis effect forces the interwell vibration responses to shift toward lower frequencies, causing the effective bandwidths of adjacent harvesters to overlap and mask distinct response peaks. These results also basically coincide with the estimation of the model shown in Fig. 12(b).

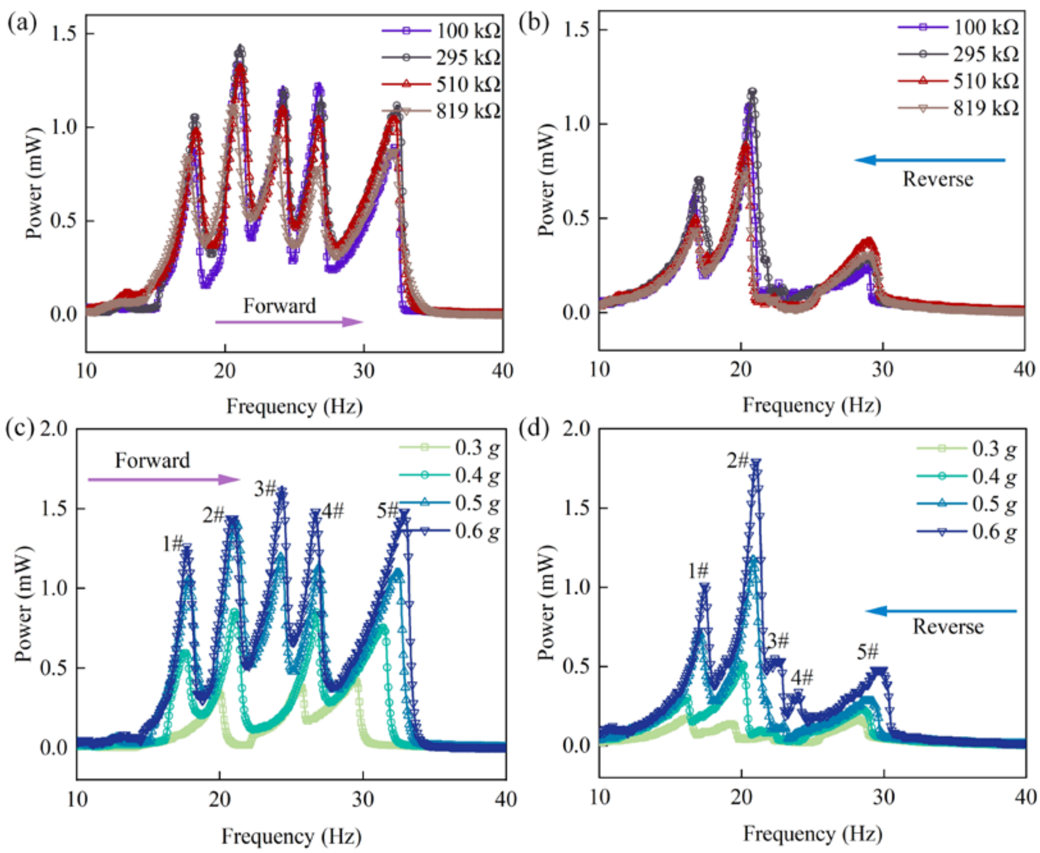

Fig. 14 The power-frequency curves of the nonlinear energy harvester array: (a) Forward sweep with different resistance loads; (b) Reverse sweep with different resistance loads; (c) Forward sweep under different excitation levels; (d) Reverse sweep under different excitation levels.

Subsequently, the load resistance was set to 295 kΩ, and various excitation levels were applied to this nonlinear energy harvester array, as illustrated in Fig. 14(c) and (d). Across both frequency sweep directions, the effective

*Corresponding author: pandiankun@nbu.edu.cn

bandwidth and output power are enhanced with increasing excitation level. When the excitation level reaches 0.6 *g*, peaks corresponding to CBPH-3# and CBPH-4# can be observed during the reverse sweep. With the reduction of excitation level, the CBPHs gradually stop functioning with interwell response, and the corresponding response peaks will vanish. However, compared to the previous design of array tuning using a tip mass [78], which required an acceleration level of 0.75 *g* to activate all CBPHs, this design represents an improvement by lowering the excitation requirement. Furthermore, experimental results under low excitation conditions reveal that deactivated CBPHs do not affect the performance of the remaining functional CBPHs. This confirms that all CBPHs in the array operate independently, and the failure of an individual CBPH does not trigger complete failure of the entire array. Accordingly, the proposed array possesses a certain degree of anti-risk capability.

A comparative analysis is added to confirm the superiority of the nonlinear array over the linear array. Fig. 15 presents the power-frequency characteristics of both arrays at 0.5 *g* acceleration. The linear array has a continuous bandwidth with five peaks corresponding to five LPBs. Three power baselines are used to define the effective frequency range for performance comparison. Defining effective bandwidth as the frequency range with power over 0.2 mW, then for the nonlinear array, the continuous effective frequency bands in the two sweeping directions are 17.6 Hz and 10.1 Hz, respectively, while the linear array measures 11.6 Hz at this baseline. When the baseline increases to 0.4 mW, the linear array’s effective range drops to 9.9 Hz, and the nonlinear array still retains 15.7 Hz in the forward sweep. At a baseline of 0.6 mW, the nonlinear array’s forward effective range reaches 9.9 Hz, around twice the linear array's effective bandwidth. These results show that the proposed nonlinear array has broader potential effective bandwidth and higher output power than the linear array.

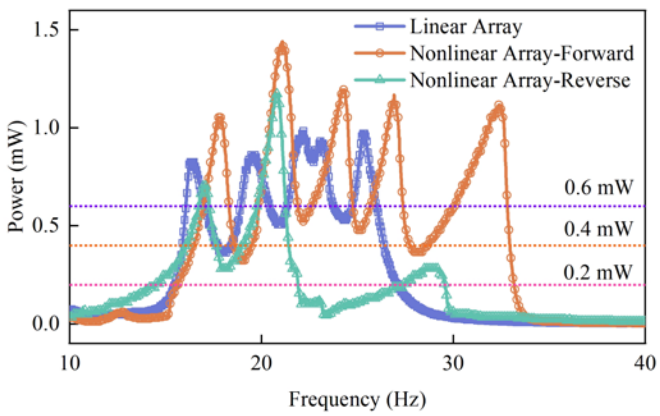

Fig. 15. Comparison of power-frequency curves at an acceleration of 0.5 *g* between the nonlinear energy harvester array and the linear energy harvester array.

However, the nonlinear array is less effective than the linear array during reverse sweep, indicating its stability is

*Corresponding author: pandiankun@nbu.edu.cn

limited by inherent nonlinear characteristics. The performance of the two arrays will be compared under random vibration to demonstrate the advantages of this nonlinear array further. Furthermore, owing to the resonant operating mode, the LPBs are prone to failure caused by PZT breakage. For instance, LPB-1# fails at an excitation level of 0.6 *g* in frequency-sweep experiments. In contrast, the CBPH can be designed with a stronger bistability to withstand higher excitation levels, which may present a potential advantage of this nonlinear array.

The performance metrics of the proposed nonlinear energy harvester array and several other nonlinear energy harvester arrays are presented in Table 5. All of these arrays have corresponding physical prototypes, with their experimental data collected by experimental measurement, and the testing protocols adopted are basically consistent. Each design has its own merits; for instance, the acceleration of the magnet-coupled mechanism is relatively low, and the bandwidth of the elastic-supported array is wide. However, the proposed array demonstrates a wider bandwidth at frequencies below 35 Hz under relatively lower acceleration. Since the harvesters in the array do not operate synchronously within the effective bandwidth, the normalized power density (NPD) of a single harvester in the array, which takes into account the peak output power, the volume of the transducers, and the excitation level, is employed for performance assessment. Owing to the small volumes of the transducers and the relatively low excitation level, the NPD of this work is relatively high. Compared with previous work, both the bandwidth and the NPD are improved. If the average power across the effective bandwidth is utilized, the NPD increases from 48.9 $mW \cdot cm^{-3} \cdot g^{-2}$ to 98.2 $mW \cdot cm^{-3} \cdot g^{-2}$, which demonstrates that the proposed array shows better power uniformity. Moreover, comparing the maximum size of the host structure in these designs, the size of the proposed array is smaller. Coupled with the advantage of not using any magnets or additional components, it features a more compact structure and is more suitable for applications in compact spaces.

Table 5. A comparison between several nonlinear energy harvester arrays and the proposed nonlinear energy harvester array

Reference	Mechanism	Maximum size (mm)	Proof mass (g)	Bandwidth (Hz)	Acceleration (g=9.8 m/s^2)	Resistance (kΩ)	NPD ($mW \cdot cm^{-3} \cdot g^{-2}$)
[71]	Piezomagnetoelastic	107×18×0.65	8.2	16.7~20	0.2	750	233.8
[83]	Magnet-coupled	79.5×10×0.27	6.5	5~14	0.36	1000	8.6
[73]	Piezomagnetoelastic	100×15×0.6	10	2~10	0.3	650	123.0
[75]	Magnet-coupled	112×10×2	7.5	49~116	1.0	—	—
[76]	Coupled by limiters	180×12.5×0.5	11.7	5.5~11.1	1.34	—	—
[77]	Coupled by supports	140×10×0.5	25.9	40~80	1.0	50	112.0
[78]	CBPH	45×8×0.2	5	13.2~26.9	0.75	290	186.7
This work	CBPH	50×7×0.25	5	15~33	0.5	295	235.0

*Corresponding author: pandiankun@nbu.edu.cn

7.4 Random vibration characterization

Most ambient vibration sources are naturally random, with energy broadly distributed across the frequency range. Therefore, random vibration measurements were conducted on this array to further characterize its performance. In these experiments, the power spectral density (PSD) of the excitation could be directly adjusted, and three PSD values (0.0005 g^2/Hz, 0.001 g^2/Hz, and 0.0015 g^2/Hz) were selected. Here, the PSD value characterizes the average acceleration statistically present within a narrow frequency band from 10 Hz to 40 Hz, which encompasses the primary operational bandwidth of the arrays. The output from each CBPH was rectified and subsequently combined through a parallel connection to a load resistance R of 295 kΩ.

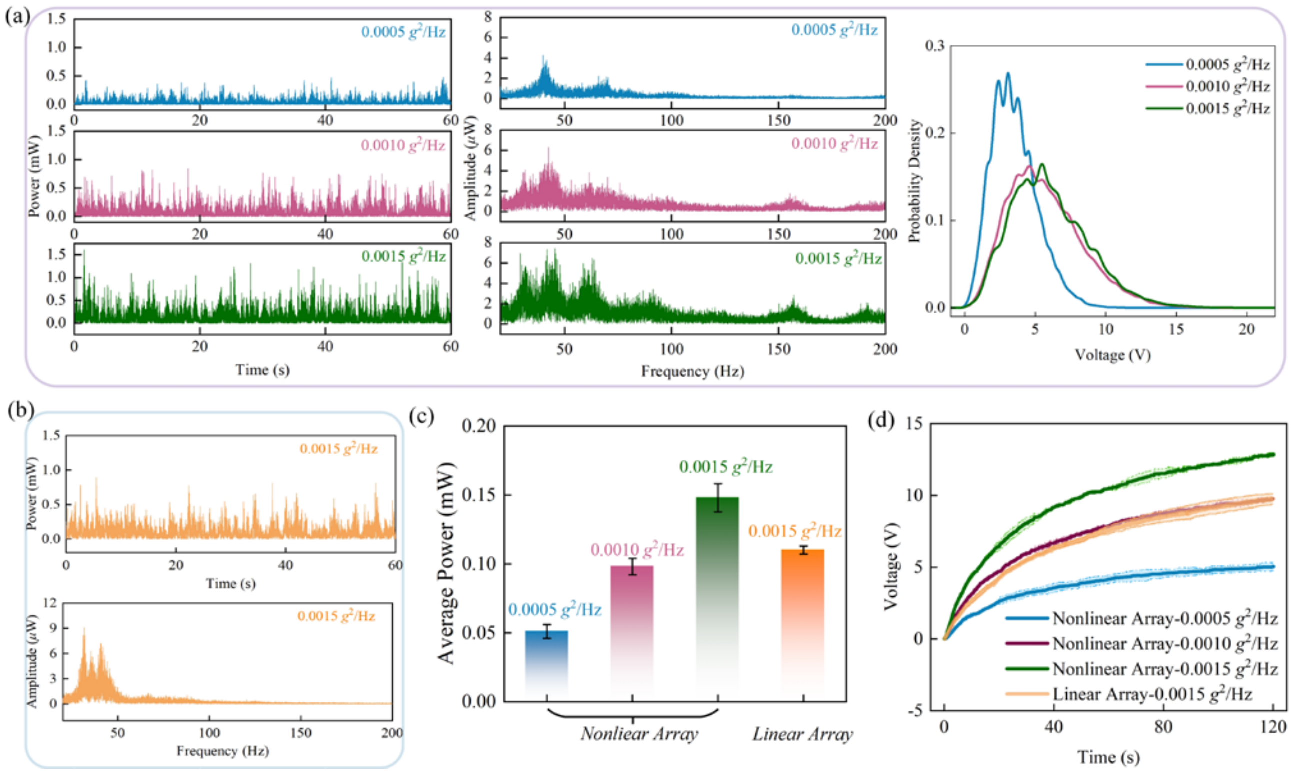

Fig. 16 The experimental results under the random vibration: (a) time-power response of the nonlinear energy harvester array and corresponding FFT plots and probability density function of voltage with different PSD values; (b) time-power response of the linear energy harvester array and corresponding FFT plot with a PSD of 0.0010 g^2/Hz; (c) the mean values and variance of the average powers of the two arrays; (d) time-voltage curves of the two arrays under the random vibration when charging a capacitor of 220 μF.

The time-domain power histories over 60 s and the corresponding FFT plots are presented in Fig. 16(a). FFT of a rectified signal produces amplitude values at even multiples of the original signal's frequency components. With an excitation frequency range of 10 Hz to 40 Hz, the resulting FFT spectrum covers 20 Hz to 80 Hz. At a PSD level of 0.0005 g^2/Hz, CBPHs are partially activated into interwell vibration mode, while full activation is achieved when the PSD reaches 0.0015 g^2/Hz. Furthermore, based on the measured voltage responses under random vibration, the

*Corresponding author: pandiankun@nbu.edu.cn

statistical form of the derived probability density function is presented in Fig. 16(a). The voltage probability density function of the proposed nonlinear energy harvester array exhibits a broad unimodal distribution with a long right tail across all tested excitation levels. As the PSD of the excitation increases, the primary peak of the distribution shifts toward higher voltage values, accompanied by a broadening of the overall distribution. This observed trend indicates that stronger random excitation increases the occurrence frequency of snap-through behaviors. Since the output voltage increases sharply with frequency on the hardening-type branch, as illustrated in Fig. 9(a), a lower output voltage can also indicate the occurrence of snap-through behavior. When 5.5 V is adopted as the threshold for identifying snap-through behavior, the corresponding probability density reaches 0.6 at a PSD level of 0.0015 g^2/Hz. This result indicates that snap-through behavior is frequently triggered under this random vibration condition.

The measurement at a PSD level of 0.0015 g^2/Hz was performed for the linear array, as shown in Fig. 16(b). It can be observed from the FFT plots that the broadband characteristic of the nonlinear array outperforms that of the linear array. The average power is determined by integrating the time-power histories. Three tests are carried out for each PSD value. The mean value of the average powers derived from these tests is statistically analyzed with the variance, as presented in Fig. 16(c). The average power of the nonlinear array increases as the PSD value rises. Moreover, it increases by 35% compared with the linear array, which is attributed to the wider bandwidth.

Moreover, the load R is replaced with a 220 μF capacitor, and the charging curves of the two arrays under this random excitation are recorded. The capacitor is charged for 120s, during which the voltage across it is continuously monitored. Three separate tests are conducted, and the average result is presented in Fig. 16(d). At the PSD level of 0.0015 g^2/Hz, the nonlinear array outperforms the linear array in both charging speed and accumulated voltage due to its wider operating bandwidth. For the nonlinear array, higher PSD levels increase both charging speed and accumulated voltage by activating more CBPHs.

To demonstrate the compatibility of this nonlinear energy harvester array with standard electronic components for energy storage, a commercial piezoelectric energy harvesting power supply circuit, LTC3588-1, is utilized to interface with the array, as illustrated in Fig. 17(a). A 100 μF capacitor is connected to the circuit input to store charge generated by the array. The voltage V_s across this capacitor is monitored, along with the output voltage V_o of the circuit. In experiments, the array is excited by random vibration with a PSD of 0.001 g^2/Hz, and the output voltage is set to 3.3 V, the typical supply voltage for electronic devices. Five LEDs are connected first, and the voltage histories of both voltages are recorded, as illustrated in Fig. 17(b). The voltage V_o initially rises as the capacitor becomes charged. When stored energy reaches the microprocessor activation threshold, the microprocessor triggers, discharges the

*Corresponding author: pandiankun@nbu.edu.cn

capacitor to light the LEDs, causing V_o to drop suddenly, while V_s shows synchronous pulsing. When PSD increases to 0.0015 g²/Hz, the pulse frequency of V_s rises, indicating more frequent LED illumination. Moreover, a low-power temperature sensor (DS18B20) is connected to the output, as illustrated in Fig. 17(c). When V_o reaches the threshold voltage, the sensor is activated, and its operating voltage V_o is stabilized at approximately 3.3 V for a short time. If the storage capacitor is increased to 220 μF, the activation time of the sensor is delayed, but the sensor can operate for a longer duration.

This proposed nonlinear energy harvester array proves the ability to broaden vibration energy harvesting, yet its potential applications are not limited to this configuration. The current design uses geometric parameters to adjust CBPH characteristics, while prior studies show modifying individual CBPH tip masses is also a viable construction approach [78]. Combining these two methods may improve the system's overall performance. Additionally, as shown in Fig. 17(d), the arrays can be mounted on a cubic support to capture vibrations from three orthogonal directions. Based on the vibration spectrum of each direction, the arrays can be customized to match the required bandwidth and load-bearing capacity. Furthermore, long-term stability and fatigue require more in-depth investigation for future practical applications.

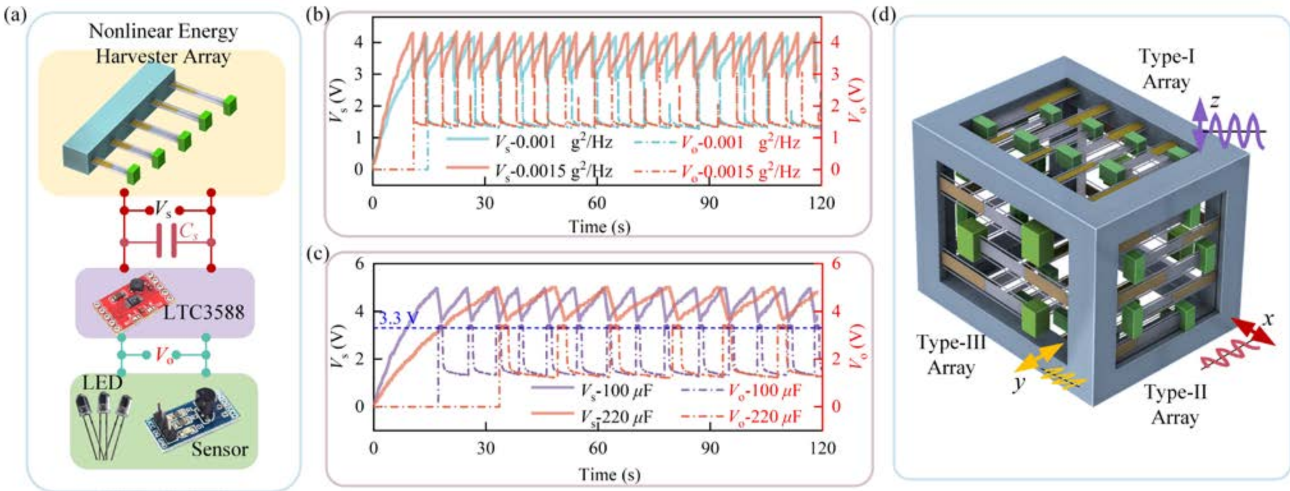

Fig. 17 (a) The diagram of the nonlinear energy harvester array for powering standard electronic components; (b) The output voltage V_s of the capacitor and the voltage V_o of converter during powering LEDs along with time; (c) The output voltage V_s of the capacitor and the converter voltage V_o of during powering the low-consumption sensor along with time; (d) The diagram of three types of nonlinear energy harvester arrays assembled on a cubic support structure to harvest vibration energy in three directions.

8. Conclusions

In this paper, a novel nonlinear energy harvester array is proposed to harvest broadband vibration energy. This array is composed of a type of cantilevered bistable piezoelectric harvester (CBPH), which is derived from the laser-machined bistable host structure without the need for magnets. These harvesters operate independently and are

*Corresponding author: pandiankun@nbu.edu.cn

designed with adjacent and interlaced bandwidths to broaden the bandwidth and to enhance the coverage of the output power across the effective bandwidth.

To establish design guidelines, a lumped-parameter analytical model is developed based on the nonlinear static mechanical characteristics of CBPHs, which is modeled using a nonlinear spring characterized by parameters k_1 and α, connected in series with a linear spring k_2, enabling control over the force-displacement response through these three stiffness coefficients. When k_2 exceeds k_1, the single force-displacement path governs the mechanical properties of the CBPH, and the corresponding bistability is relatively weak.

To validate the feasibility of the model, the dynamic performance of the CBPH is systematically investigated, and the transition of the primary response type from the softening type to the hardening type with the increase of excitation is found. The desired hardening-type response with interwell vibrations for energy harvesting can be more readily achieved at a low excitation level. Additionally, output power is nonuniformly distributed across the effective bandwidth of the hardening-type branch.

A parametric analysis is conducted with the assistance of the finite element method to lay a foundation for design guidelines. It has been found that the width W_2 of the supporting beams can modify the buckling degree of the main beam without altering the mechanical properties induced by the cantilever boundary. However, the remaining parameters will change both mechanical properties simultaneously.

Guided by these findings, a nonlinear broadband energy harvester array integrating five CBPHs is designed and experimentally evaluated, and its performance is further compared with that of a conventional linear energy harvester array. This array achieves a continuous operational bandwidth ranging from 15 Hz to 33 Hz under 0.5 g excitation with an average output power of 0.65 mW across the bandwidth, which is almost half of the peak power, and exhibits a better uniformity of power distribution than the single CBPH. Then, random vibration tests confirm that the nonlinear array outperforms linear arrays in key functionalities, including charging capacitors and powering standard electronic components, verifying its ability to effectively adapt to various environmental vibration conditions.

Furthermore, the proposed design strategy allows customizing nonlinear energy harvester arrays based on excitation level. This can serve as an alternative power solution for wireless sensor networks in space-constrained, magnet-sensitive scenarios, especially those dominated by low-frequency variable-amplitude vibrations.

Acknowledgement

This work was supported by the National Natural Science Foundation of China [grant No. 12202215] and the Ningbo Natural Science Foundation [grant No. 2024J189].

*Corresponding author: pandiankun@nbu.edu.cn

References

[1] Singh J, Kaur R, Singh D. Energy harvesting in wireless sensor networks: A taxonomic survey. International Journal of Energy Research. 2021;45:118-40.

[2] Sanislav T, Mois GD, Zeadally S, Folea SC. Energy Harvesting Techniques for Internet of Things (IoT). IEEE Access. 2021;9:39530-49.

[3] Zeadally S, Shaikh FK, Talpur A, Sheng QZ. Design architectures for energy harvesting in the Internet of Things. Renewable and sustainable energy reviews. 2020;128:109901.

[4] Kraśny MJ, Bowen CR. A system for characterisation of piezoelectric materials and associated electronics for vibration powered energy harvesting devices. Measurement. 2021;168:108285.

[5] He Q, Briscoe J. Piezoelectric Energy Harvester Technologies: Synthesis, Mechanisms, and Multifunctional Applications. ACS Applied Materials & Interfaces. 2024;16:29491-520.

[6] Pan X, Wu Y, Wang Y, Zhou G, Cai H. Mechanical energy harvesting based on the piezoelectric materials: Recent advances and future perspectives. Chemical Engineering Journal. 2024;497:154249.

[7] Wei C, Jing X. A comprehensive review on vibration energy harvesting: Modelling and realization. Renewable and sustainable energy reviews. 2017;74:1-18.

[8] Sezer N, Koç M. A comprehensive review on the state-of-the-art of piezoelectric energy harvesting. Nano Energy. 2021;80:105567.

[9] Safaei M, Sodano HA, Anton SR. A review of energy harvesting using piezoelectric materials: state-of-the-art a decade later (2008–2018). Smart Materials and Structures. 2019;28:113001.

[10] Sun Y, Han Q, Jiang T, Li C. Coupled bandgap properties and wave attenuation in the piezoelectric metamaterial beam on periodic elastic foundation. Applied Mathematical Modelling. 2024;125:293-310.

[11] Zou H-X, Zhao L-C, Gao Q-H, Zuo L, Liu F-R, Tan T, et al. Mechanical modulations for enhancing energy harvesting: Principles, methods and applications. Applied Energy. 2019;255:113871.

[12] Xiao Y, Han Q, Wu N. Piezoelectric energy harvesting: a review of energy sources, structures, and working mechanisms in high-frequency excitations and operations. Smart Materials and Structures. 2025;34:023001.

[13] Zhang B, Zhao Z, Li Y, Zhang X, Li X, Hao D, et al. Design and analysis of a piezoelectric energy harvesting shock absorber for light truck applications. Applied Energy. 2025;377:124569.

[14] Gholikhani M, Roshani H, Dessouky S, Papagiannakis AT. A critical review of roadway energy harvesting technologies. Applied Energy. 2020;261:114388.

[15] Zhou Z, Cao D, Huang H, Qin W. Efficiently harvesting low-speed wind energy by a novel bi-stable piezoelectric energy harvester from vortex-induced vibration and galloping. Mechanical Systems and Signal Processing. 2024;209:111124.

[16] Ali A, Ali S, Shaukat H, Khalid E, Behram L, Rani H, et al. Advancements in piezoelectric wind energy harvesting: A review. Results in Engineering. 2024;21:101777.

[17] Wang J, Xiang H, Jing H, Zhu Y, Zhang Z. Stochastic analysis for vortex-induced vibration piezoelectric energy harvesting in incoming wind turbulence. Applied Energy. 2025;377:124618.

[18] Fang S, Wang X, Zhang X, Wu K, Yan T, Chuai X, et al. High output, lightweight and small-scale rotational piezoelectric energy harvester utilizing internal impact effect. Energy Conversion and Management. 2024;322:119180.

[19] Tian H, Yurchenko D, Li Z, Guo J, Kang X, Wang J. Dumbbell-shaped piezoelectric energy harvesting from coupled vibrations. International Journal of Mechanical Sciences. 2024;281:109681.

[20] Xue X, Xiang H, Ci Y, Wang J. A sustainable galloping piezoelectric energy harvesting wind barrier for power generation on railway bridges. Energy. 2025;320:135135.

[21] Goldschmidtboeing F, Woias P. Characterization of different beam shapes for piezoelectric energy harvesting. Journal

*Corresponding author: pandiankun@nbu.edu.cn

of micromechanics and microengineering. 2008;18:104013.
[22] Wakshume DG, Płaczek MŁ. Optimizing Piezoelectric Energy Harvesting from Mechanical Vibration for Electrical Efficiency: A Comprehensive Review. Electronics2024.
[23] Yang P, Ahmad Mazlan AZ. Experimental study on long-term fatigue behavior of piezoelectric energy harvesters under high and low-frequency vibration excitation. International Journal of Fatigue. 2025;194:108817.
[24] Yildirim T, Ghayesh MH, Li W, Alici G. A review on performance enhancement techniques for ambient vibration energy harvesters. Renewable and sustainable energy reviews. 2017;71:435-49.
[25] Wu S, Kan J, Wu W, Lin S, Yu Y, Liao W, et al. A tunable pendulum-like piezoelectric energy harvester for multidirectional vibration. Sustainable Materials and Technologies. 2024;41:e01094.
[26] Sugino C, Erturk A. Analysis of multifunctional piezoelectric metastructures for low-frequency bandgap formation and energy harvesting. Journal of Physics D: Applied Physics. 2018;51:215103.
[27] Izadgoshasb I, Lim YY, Vasquez Padilla R, Sedighi M, Novak JP. Performance Enhancement of a Multiresonant Piezoelectric Energy Harvester for Low Frequency Vibrations. Energies. 2019;12:2770.
[28] Wang G, Song R, Luo L, Yu P, Yang X, Zhang L. Multi-piezoelectric energy harvesters array based on wind-induced vibration: Design, simulation, and experimental evaluation. Energy. 2024;300:131509.
[29] Dong K, Jiang L, Ding B. Performances Investigation of Multi-Configuration Connections in Piezoelectric Energy Harvester. Journal of Vibration Engineering & Technologies. 2025;13:16.
[30] Ma X, Gong L, Zeng Z, Wu Y, Guo W, Chen H, et al. Design and optimization of a compact broadband piezoelectric energy harvester system with enhanced efficiency. Renewable Energy. 2025;247:122935.
[31] Fan Y, Zhang Y, Niu M-Q, Chen L-Q. An internal resonance piezoelectric energy harvester based on geometrical nonlinearities. Mechanical Systems and Signal Processing. 2024;211:111176.
[32] Xing J, Ji X, Wu J, Howard I. A body hair-inspired multi-directional piezoelectric energy harvester with spatial internal resonance effect. Journal of Sound and Vibration. 2024;589:118543.
[33] Daraghma H, Jaber N, Hawwa M. Exploiting internal resonance of 3D-printed weakly coupled structures for piezoelectric energy harvesting. Nonlinear Dynamics. 2024;112:16847-69.
[34] Li X-Y, Huang IC, Su W-J. Analysis of a two-degree-of-freedom beam for rotational piezoelectric energy harvesting. Mechanical Systems and Signal Processing. 2025;223:111899.
[35] Xie Z, Xiong J, Zhang D, Wang T, Shao Y, Huang W. Design and Experimental Investigation of a Piezoelectric Rotation Energy Harvester Using Bistable and Frequency Up-Conversion Mechanisms. Applied Sciences. 2018;8.
[36] Fu H, Yeatman EM. Rotational energy harvesting using bi-stability and frequency up-conversion for low-power sensing applications: Theoretical modelling and experimental validation. Mechanical Systems and Signal Processing. 2019;125:229-44.
[37] Zhang P, Lin W, Xie Z, Cao H, Huang W. L-shaped cantilever beam piezoelectric energy harvester with frequency up-conversion for ultra-low-frequency rotating environments. Mechanical Systems and Signal Processing. 2025;225:112281.
[38] Shen J, Wan S, Fu J, Li S, Lv D, Dekemele K. A magnetic plucking frequency up-conversion piezoelectric energy harvester with nonlinear energy sink structure. Applied Energy. 2024;376:124326.
[39] Leland ES, Wright PK. Resonance tuning of piezoelectric vibration energy scavenging generators using compressive axial preload. Smart Materials and Structures. 2006;15:1413.
[40] Wang X, Chen C, Wang N, San H, Yu Y, Halvorsen E, et al. A frequency and bandwidth tunable piezoelectric vibration energy harvester using multiple nonlinear techniques. Applied Energy. 2017;190:368-75.
[41] Hu Y, Xue H, Hu H. A piezoelectric power harvester with adjustable frequency through axial preloads. Smart Materials and Structures. 2007;16:1961.
[42] Zhang H, Chen S, Karimi M, Li B, Saydam S, Hassan M. Numerical and experimental investigation of an auxetic piezoelectric energy harvester with frequency self-tuning capability. Smart Materials and Structures. 2024;33:055022.

*Corresponding author: pandiankun@nbu.edu.cn

[43] Yuan Z, Liu W, Zhang S, Zhu Q, Hu G. Bandwidth broadening through stiffness merging using the nonlinear cantilever generator. Mechanical Systems and Signal Processing. 2019;132:1-17.
[44] Zhang H-b, Chen Y-b, Li K-k, Wang Y-f, Wang G-q. Piezoelectric energy harvester with tip 3D-printed bi-stable asymmetric raceway for effective harvesting of ultralow-frequency and low-level vibration energy. Mechanical Systems and Signal Processing. 2025;224:112054.
[45] Elgamal MA, Elgamal H, Kouritem SA. Optimized multi-frequency nonlinear broadband piezoelectric energy harvester designs. Scientific Reports. 2024;14:11401.
[46] Hou C, Shan X, Dang S, Du X, Sui G, Xie T. A magnetically excited broadband rotary piezoelectric energy harvester with nonlinear energy sink: Theoretical investigations and experimental Verifications. Mechanical Systems and Signal Processing. 2025;224:112085.
[47] Liu Q, Liu H, Zhang J. Optimization of nonlinear energy sink using Euler-buckled beams combined with piezoelectric energy harvester. Mechanical Systems and Signal Processing. 2025;223:111812.
[48] Chen H-H, You S-K, Su W-J. The design, fabrication and analysis of a cantilever-based tensile-mode nonlinear piezoelectric energy harvester. Mechanical Systems and Signal Processing. 2024;212:111317.
[49] Liu J-Q, Fang H-B, Xu Z-Y, Mao X-H, Shen X-C, Chen D, et al. A MEMS-based piezoelectric power generator array for vibration energy harvesting. Microelectronics Journal. 2008;39:802-6.
[50] Wang W, Yang T, Chen X, Yao X. Vibration energy harvesting using a piezoelectric circular diaphragm array. IEEE transactions on ultrasonics, ferroelectrics, and frequency control. 2012;59:2022-6.
[51] Kirubaveni S, Radha S, Sreeja BS, Sivanesan T. Analysis of rectangular and triangular end array type piezoelectric vibration energy harvester. Microsystem technologies. 2015;21:2165-73.
[52] Upadrashta D, Yang Y. Trident-Shaped Multimodal Piezoelectric Energy Harvester. Journal of Aerospace Engineering. 2018;31:04018070.
[53] Kouritem SA, Al-Moghazy MA, Noori M, Altabey WA. Mass tuning technique for a broadband piezoelectric energy harvester array. Mechanical Systems and Signal Processing. 2022;181:109500.
[54] Zhou S, Cao J, Lin J. Theoretical analysis and experimental verification for improving energy harvesting performance of nonlinear monostable energy harvesters. Nonlinear Dynamics. 2016;86:1599-611.
[55] Fan K, Tan Q, Liu H, Zhang Y, Cai M. Improved energy harvesting from low-frequency small vibrations through a monostable piezoelectric energy harvester. Mechanical Systems and Signal Processing. 2019;117:594-608.
[56] Fu J, Zeng X, Wu N, Wu J, He Y, Xiong C, et al. Design, modeling and experiments of bistable piezoelectric energy harvester with self-decreasing potential energy barrier effect. Energy. 2024;300:131572.
[57] Dang S, Hou C, Shan X, Sui G, Zhang X. A novel T-shaped beam bistable piezoelectric energy harvester with a moving magnet. Energy. 2024;300:131486.
[58] Wang M, Wu H, Zhang J, Yang Y, Ding J, Sun Y, et al. Multi-magnet coupled bistable piezoelectric energy harvesters for performance enhancement. Energy. 2024;306:132452.
[59] Plagianakos TS, Leventakis N, Chrysochoidis NA, Kardarakos G-C, Margelis N, Bolanakis G, et al. Piezoelectric energy harvester for wind turbine blades based on bistable response of a composite beam in post-buckling. Smart Materials and Structures. 2024;33:075033.
[60] Taufan I, Punch J, Nico V. A tunable and bistable piezoelectric vibrational energy harvester with a compliant ortho-planar spring and buckled H-I structure. European Journal of Mechanics - A/Solids. 2026;119:106151.
[61] Cui D, Shang H. Global dynamic analysis of a typical tristable piezoelectric energy harvester for performance enhancement. Chaos, Solitons & Fractals. 2024;186:115277.
[62] Wang T, Zhang Q, Han J, Tian R, Yan Y, Cao X, et al. Low-frequency energy scavenging by a stacked tri-stable piezoelectric energy harvester. International Journal of Mechanical Sciences. 2024;280:109546.
[63] Zhi Y, Li X, Zhang J, Zhang L, Li J, Zhao W, et al. A novel tri-stable piezoelectric vibration energy harvester with an

*Corresponding author: pandiankun@nbu.edu.cn

elastic boundary. Mechanical Systems and Signal Processing. 2025;228:112504.

[64] Man D, Jiang B, Zhang Y, Tang L, Xu Q, Chen D, et al. A Hybrid Tri-Stable Piezoelectric Energy Harvester with Asymmetric Potential Wells for Rotational Motion Energy Harvesting Enhancement. Energies2024.

[65] Fan Y, Liu X, Wang DF. A hummingbird-inspired dual-oscillator synergized piezoelectric energy harvester for ultra-low frequency. Mechanical Systems and Signal Processing. 2025;224:112132.

[66] Zhang X, Huang X, Wang B. A quad-stable nonlinear piezoelectric energy harvester with piecewise stiffness for broadband energy harvesting. Nonlinear Dynamics. 2024;112:19633-52.

[67] Wang Z, Shang H. Multistability Mechanisms for Improving the Performance of a Piezoelectric Energy Harvester with Geometric Nonlinearities. Fractal and Fractional2024.

[68] Fang S, Zhou S, Yurchenko D, Yang T, Liao W-H. Multistability phenomenon in signal processing, energy harvesting, composite structures, and metamaterials: A review. Mechanical Systems and Signal Processing. 2022;166:108419.

[69] Sun W-P, Su W-J. Design and analysis of an extended buckled beam piezoelectric energy harvester subjected to different axial preload. Smart Materials and Structures. 2024;33:055007.

[70] Li Q, Wang C, Liu C, Li Z, liu X, He L. Development Trend of Nonlinear Piezoelectric Energy Harvesters. Journal of Electronic Materials. 2025;54:1-23.

[71] Upadrashta D, Yang Y. Nonlinear piezomagnetoelastic harvester array for broadband energy harvesting. Journal of Applied Physics. 2016;120.

[72] Deng H, Du Y, Wang Z, Ye J, Zhang J, Ma M, et al. Poly-stable energy harvesting based on synergetic multistable vibration. Communications Physics. 2019;2:21.

[73] Lai S-K, Wang C, Zhang L-H. A nonlinear multi-stable piezomagnetoelastic harvester array for low-intensity, low-frequency, and broadband vibrations. Mechanical Systems and Signal Processing. 2019;122:87-102.

[74] Mei X, Nan H, Dong R, Zhou R, Jin J, Sun F, et al. Magnetic-linkage nonlinear piezoelectric energy harvester with time-varying potential wells: Theoretical and experimental investigations. Mechanical Systems and Signal Processing. 2024;208:110998.

[75] Xie X, Zhang J, Wang Z, Li L, Du G. The effect of magnetic proof masses on the energy harvesting bandwidth of piezoelectric coupled cantilever array. Applied Energy. 2024;353:122042.

[76] Fan Y, Ghayesh MH, Lu T-F, Amabili M. Design, development, and theoretical and experimental tests of a nonlinear energy harvester via piezoelectric arrays and motion limiters. International Journal of Non-Linear Mechanics. 2022;142:103974.

[77] Shim H-K, Sun S, Kim H-S, Lee D-G, Lee Y-J, Jang J-S, et al. On a nonlinear broadband piezoelectric energy harvester with a coupled beam array. Applied Energy. 2022;328:120129.

[78] Pan D, Liang Y, Zhang Z, Wu Z. Design and dynamics of a cantilevered bistable buckled piezoelectric beam for vibrational energy harvesting. Mechanical Systems and Signal Processing. 2025;224:112013.

[79] Jiang L, Dong K, Ding B. Design and investigation of a compliant-pneumatic quasi-zero stiffness device for energy harvesting. Smart Materials and Structures. 2025;34:085028.

[80] Pan D, Wu Z, Dai F, Tolou N. A novel design and manufacturing method for compliant bistable structure with dissipated energy feature. Materials & Design. 2020;196:109081.

[81] Bazant Z, Cedolin L. Stability of Structures: Elastic, Inelastic, Fracture and Damage Theories1991.

[82] Pan D, Dai F. Design and analysis of a broadband vibratory energy harvester using bi-stable piezoelectric composite laminate. Energy Conversion and Management. 2018;169:149-60.

[83] Zhou S, Cao J, Wang W, Liu S, Lin J. Modeling and experimental verification of doubly nonlinear magnet-coupled piezoelectric energy harvesting from ambient vibration. Smart Materials and Structures. 2015;24:055008.

*Corresponding author: pandiankun@nbu.edu.cn